

1 **eLife – Research Article**

2 **T cells modulate the microglial response to brain ischemia**

3

4 Corinne Benakis<sup>\*1</sup>, Alba Simats<sup>1</sup>, Sophie Tritschler<sup>3</sup>, Steffanie Heindl<sup>1</sup>, Simon Besson-Girard<sup>1</sup>,  
5 Gemma Llovera<sup>1</sup>, Kelsey Pinkham<sup>1</sup>, Anna Kolz<sup>4</sup>, Fabian Theis<sup>3</sup>, Özgün Gökce<sup>1,2</sup>, Anneli Peters<sup>4,5</sup>,  
6 Arthur Liesz<sup>\*1,2</sup>

7

8 <sup>1</sup>Institute for Stroke and Dementia Research (ISD), University Hospital, LMU Munich 81377 Munich,  
9 Germany

10 <sup>2</sup>Munich Cluster for Systems Neurology (SyNergy), Munich, Germany

11 <sup>3</sup>Institute of Diabetes and Regeneration Research, Helmholtz Zentrum München, 85764 Neuherberg,  
12 Germany; Institute of Computational Biology, Helmholtz Zentrum München

13 <sup>4</sup>Institute of Clinical Neuroimmunology, University Hospital, LMU Munich, 82152 Planegg-Martinsried,  
14 Germany

15 <sup>5</sup>Biomedical Center (BMC), Faculty of Medicine, LMU Munich, 82152 Planegg-Martinsried, Germany

16

17 \*Shared corresponding authors:

18 Corinne Benakis

19 Institute for Stroke and Dementia Research (ISD)

20 LMU Klinikum

21 Feodor-Lynen-Strasse 17

22 81373 Munich, Germany

23 Phone: +49 89 4400 46205

24 E-mail: Corinne.Benakis@med.uni-muenchen.de

25

26 And

27

28 Arthur Liesz

29 Institute for Stroke and Dementia Research (ISD)

30 LMU Klinikum

31 Feodor-Lynen-Strasse 17

32 81373 Munich, Germany

33 Phone: +49 89 4400 46169

34 E-mail: Arthur.Liesz@med.uni-muenchen.de

35

36 **Keywords** Stroke, Microglia, T cells, single-cell transcriptomics

37

38

39 **Summary**

40 The crosstalk between brain infiltrating T cells and microglia in response to stroke remains elusive.  
41 Benakis et al. report that transcriptional signature of the stroke-associated microglia is reprogrammed  
42 by distinct T cell subpopulations. Engineered T cells overexpressing IL-10 administered four hours after  
43 stroke reinitiate microglial function inducing a pro-regenerative environment.

44

45 **Abstract**

46 Neuroinflammation after stroke is characterized by the activation of resident microglia and the invasion  
47 of circulating leukocytes into the brain. Although lymphocytes infiltrate the brain in small number, they  
48 have been consistently demonstrated to be the most potent leukocyte subpopulation contributing to  
49 secondary inflammatory brain injury. However, the exact mechanism how this minimal number of  
50 lymphocytes can profoundly affect stroke outcome is still largely elusive. Here, using a mouse model  
51 for ischemic stroke, we demonstrated that early activation of microglia in response to stroke is  
52 differentially regulated by distinct T cell subpopulations. Acute treatment with engineered T cells  
53 overexpressing IL-10 administered into the cisterna magna after stroke induces a switch of microglial  
54 gene expression to a profile associated with pro-regenerative functions. These findings substantiate  
55 the role of T cells in stroke with large impact on the cerebral inflammatory milieu by polarizing the  
56 microglial phenotype. Targeting T cell-microglia interactions can have direct translational relevance for  
57 further development of immune-targeted therapies for stroke and other neuroinflammatory conditions.

58

59 **Introduction**

60 Among peripheral leukocytes invading the injured brain, T cells have been consistently identified as the  
61 invading leukocyte subpopulation with the largest impact on secondary neurodegeneration and  
62 modulation of the ischemic brain damage (Kleinschnitz et al., 2010; Liesz et al., 2011, 2009). T cell  
63 subpopulations have the potential to play either a neuroprotective or a deleterious role in post-stroke  
64 neuroinflammation. In particular, the pro-inflammatory  $T_{H1}$ ,  $T_{H17}$  subsets of  $T_{\text{HELPER}}$  cells and IL-17-  
65 producing  $\gamma\delta$  T cells have been shown to induce secondary neurotoxicity, leading to infarct expansion  
66 with worse functional outcome (Gelderblom et al., 2012; Shichita et al., 2009), whereas regulatory T  
67 cells ( $T_{\text{REG}}$ ) exert anti-inflammatory and neuroprotective function suppressing an excessive  
68 inflammatory reaction to the brain infarct (Liesz et al., 2009). Recruitment of peripheral immune cells  
69 is not limited to the brain parenchyma since an accumulation of T cells is observed in the choroid plexus  
70 and the meninges after stroke (Benakis et al., 2016; Llovera et al., 2017). Attempt in blocking the  
71 recruitment of peripheral effector T cells diminished neuronal damage in different cerebral ischemic  
72 models, resulting in improvement of stroke outcome and suggesting a possible therapeutic target  
73 (Liesz et al., 2011; Llovera et al., 2015). Considering the relatively low number of only a few thousand  
74 lymphocytes invading the brain after stroke compared to more than fifty times higher cell count of  
75 innate immune cells (invading and resident) in the post-stroke brain (Gelderblom et al., 2009), it is  
76 surprising to observe such a dramatic effect of a small number of T cells on the neuroinflammatory  
77 response to stroke.

78 Therefore, we hypothesized that T cells have a polarizing effect on microglial function. In turn, microglia  
79 – as the most abundant immune cell population in the ischemic brain – could amplify the T cells' impact  
80 on the cerebral immune milieu. Indeed, microglia interact with T cells via either cell-to-cell contact,  
81 cytokine-mediated communication or antigen presentation leading to activation/polarization of  
82 adaptive immune cells entering the brain (Goldmann and Prinz, 2013). T cell–microglia interaction can  
83 further influence the neuroinflammatory response in experimental models of multiple sclerosis (Dong  
84 and Yong, 2019) and possibly in stroke (Wang et al., 2016). In fact, recent evidence suggest a crosstalk  
85 between microglia and T cells as a key determinant of neuronal plasticity during recovery from brain  
86 injury (Shi et al., 2021). However, while the influence of microglia/macrophages on T cells has been  
87 well-studied, it is still unclear how in reverse the T cells influence microglial function, and whether early  
88 interaction of T cells with microglia in the acute response to stroke can have an immediate impact on  
89 microglia and further change the course of disease progression.

90 Using single-cell sequencing and adoptive transfer models of *ex vivo* differentiated  $T_{\text{HELPER}}$  cell  
91 subpopulations, we performed an in-depth analysis of the immunomodulatory effects of T cells on  
92 microglial polarization. Better understanding of the T cell–microglia crosstalk holds the potential to use  
93 polarized T cells as a therapeutic approach with large impact on the cerebral inflammatory milieu  
94 potentiated by resident microglia.

95

96

97 **Results**

98 **Lymphocytes modulate the activation state of microglia in response to stroke**

99 First, we investigated the effect of lymphocytes on microglial morphology and transcriptome in  
100 lymphocyte-deficient *Rag1<sup>-/-</sup>* mice after experimental stroke (**Fig. 1a**). Microglia were analyzed 5 days  
101 after stroke because this acute time point has previously been identified as the time of maximal  
102 cerebral lymphocyte infiltration in the same stroke model (Llovera et al., 2017). Using an automated  
103 morphological analysis of IBA1 positive cells (Heindl et al., 2018), we identified that microglia in the  
104 perilesional (ipsilateral) cortex of *Rag1<sup>-/-</sup>* mice displayed extended ramifications and a lower sphericity  
105 compared to microglia of wild type (WT) mice, indicating a less activated microglial phenotype in the  
106 absence of lymphocytes (**Fig. 1b, c**). In contrast, microglial morphology remained unchanged between  
107 *Rag1<sup>-/-</sup>* and WT mice in the contralateral (unaffected) hemisphere which does not show recruitment of  
108 lymphocyte in considerable amounts, supporting the role of local lymphocyte infiltration for changing  
109 microglial morphology. Therefore, we investigated the functional implications of cerebral lymphocyte  
110 invasion for microglia by single-cell transcriptomics in WT and *Rag1<sup>-/-</sup>* mice. CD45<sup>+</sup>CD11b<sup>+</sup> myeloid cells  
111 were sorted by flow cytometry from naïve mice or 5 days after stroke (pool of 3 mice per condition) and  
112 single-cell RNA sequencing was performed using 10x Genomics (**Fig. 1d**). Unsupervised clustering  
113 analysis identified 14 distinct clusters across conditions (**Fig. 1e** and Supplementary Fig. 1a). Based on  
114 the expression of previously defined markers of homeostatic and reactive microglia per cell cluster  
115 (gene expression of *Fcrls*, *P2ry12*, *Trem2*; absence of *Lyz2*, *Ccr2*; (Keren-Shaul et al., 2017; Miron and  
116 Priller, 2020; Prinz and Priller, 2014)), 5 clusters were annotated as microglial cells (**Fig. 1e, right**, and  
117 Supplementary Fig. 1a). We then further clustered the microglial cells into subpopulations showing  
118 either a transcriptomic profile associated with homeostatic microglial function (clusters 0, 1, 4, 6) or a  
119 profile of reactive microglia, activated in response to the ischemic tissue injury (clusters 2, 3, 5, 7)  
120 (Supplementary Fig. 1b, c). The cell distribution across condition highlighted that stroke induced a  
121 reactive transcriptomic profile in the majority of microglia derived from the perilesional cortex, both in  
122 WT and *Rag1<sup>-/-</sup>* mice (**Fig. 1f**).

123 The microglial reaction to stroke causes a gradual shift from the homeostatic transcriptomic profile to  
124 a reactive state. In order to capture differences in the microglia transcriptome along its transition phase,  
125 we performed single cell trajectory inference analysis (Supplementary Fig. 2). Partition-based graph  
126 abstraction (PAGA) revealed two distinct paths with high connectivity from the homeostatic (naïve)  
127 microglia cluster (root cluster) to the reactive (stroke) microglia cluster (end cluster) (Supplementary  
128 Fig. 2a). Interestingly, the number of microglial cells in stroke *Rag1<sup>-/-</sup>* increased in the end cluster and  
129 was decreased along the trajectory path 2 in comparison to stroke WT (Supplementary Fig. 2b),  
130 suggesting that lymphocytes influence the transition of a microglia subpopulation from the  
131 homoeostatic to the reactive state. Differential gene expression analysis between the root and end  
132 clusters of the trajectory path 2 in WT and *Rag1<sup>-/-</sup>* mice (Supplementary Fig. 2c) revealed that genes  
133 associated with ribosomal metabolic processes and mitochondrial ribosomal proteins were specifically  
134 enriched whereas genes associated with phagocytosis were down-regulated in microglia of *Rag1<sup>-/-</sup>*  
135 mice (Supplementary Fig. 2d). We then clustered genes into groups of correlating and anti-correlating

136 genes and investigated the activation of these gene sets along the identified trajectory path 2 in stroke  
 137 condition only (Supplementary Fig. 1d-f). Gene sets which were significantly different between WT and  
 138  $Rag1^{-/-}$  mice after stroke revealed that the absence of lymphocytes significantly reduces microglial  
 139 genes associated with macrophage activation state (G6: *Foxp1*, *Syk*), whereas genes associated with  
 140 cytokine/chemokine stimulus were enriched (G3: *Il1b*, *Tnf*, *Csf1*, *Ccl2*) in  $Rag1^{-/-}$  in comparison to WT  
 141 microglia (**Fig 1g**).

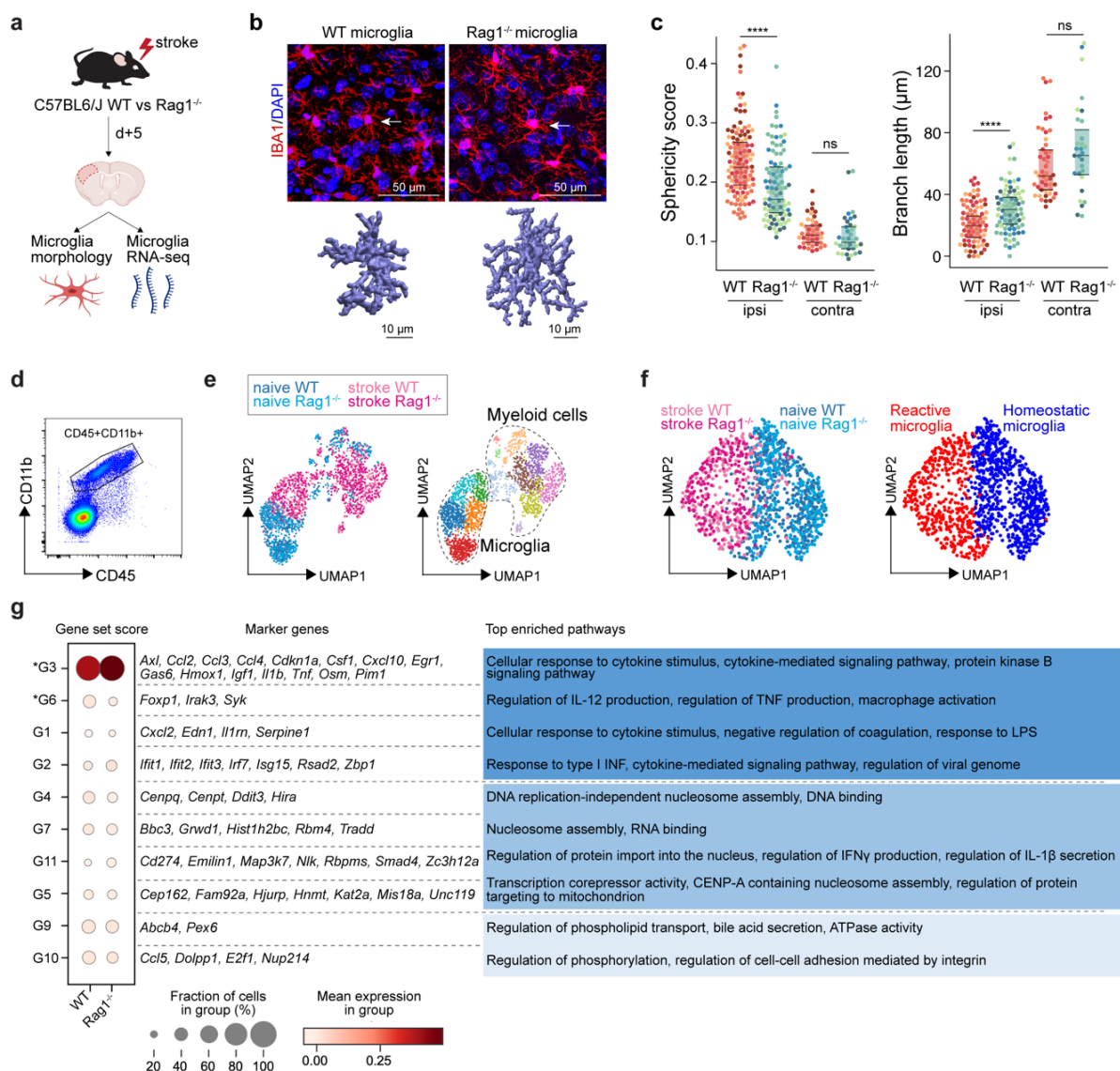


**Figure 1. T cells influence microglia morphology and transcriptomic signature.** **a** Morphological analysis of microglia and transcriptomic profile of sorted microglia were performed 5 d after stroke in wild-type (WT) and  $Rag1^{-/-}$  mice. **b** Top, representative images of IBA1+ microglial cells in the perilesional region (900  $\mu$ m distal to the infarct border, cortical layer 4). Bottom, three-dimensional (3D) reconstruction of microglia in WT and  $Rag1^{-/-}$  mice. **c** Morphological analysis of microglia in the peri-infarct area (ipsi) and in the contralateral hemisphere (contra) for two representative features: sphericity and branch length ( $\mu$ m) in WT (orange) and  $Rag1^{-/-}$  (blue) mice. Each individual mouse is represented in the plots by one color (4 mice/condition), each dot corresponds to one microglial cell; ns, non significant; \*\*\*\*,  $P < 0.0001$ . Wilcoxon rank sum test with continuity correction and Bonferroni post-hoc correction for multiple testing. **d** CD45+CD11b+ cells were sorted from the ipsilateral hemisphere 5 d after stroke in WT and  $Rag1^{-/-}$  (3 mice/condition) and RNA was isolated for single cell RNA sequencing (10x Genomics). **e** Uniform manifold approximation and projection 2D space (UMAP) plots of 2345 CD45+CD11b+ cells colored by conditions (left) and by 14 distinct transcriptional clusters (right and Supplementary Fig. 1). **f** Clustering of the microglia subset color-coded by conditions (left) and into homeostatic and reactive microglia (right). **g** Selected gene sets of highly correlated and anti-correlated genes based on trajectory inference analysis in stroke condition (Supplementary Fig. 1d-f). Mean gene set activation score in WT and  $Rag1^{-/-}$  cells, selected marker genes and top enriched gene ontology pathways associated to each gene set. Gene sets were classified by p-value (the lowest p-value at the top, asterisks (\*) indicate significant difference between genotype in stroke condition) and by similar pathways, such as: pathways related to inflammation (dark blue), pathways related to DNA/RNA regulation (blue) and lipid pathways (light blue).

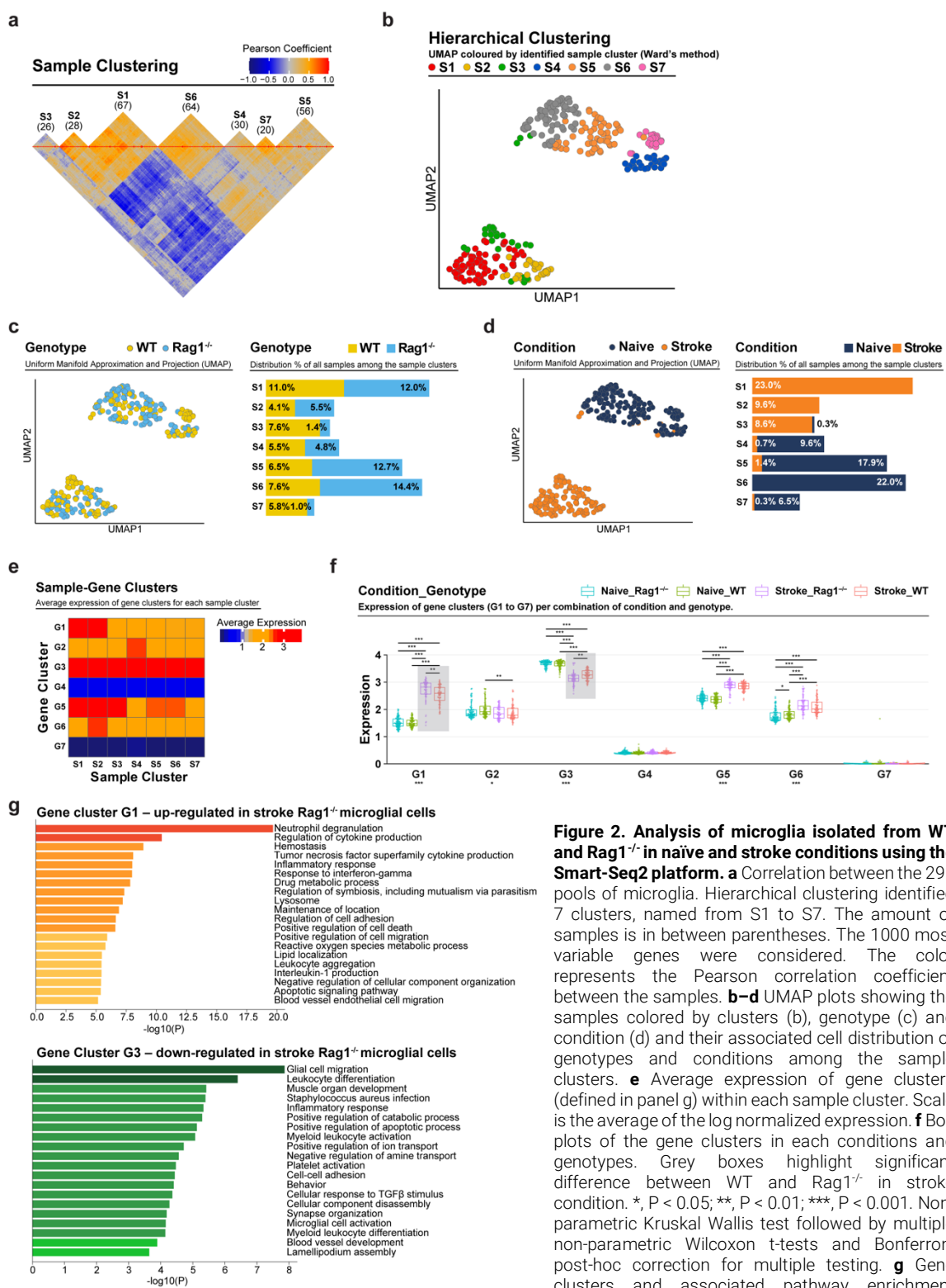


**Figure 2. Analysis of microglia isolated from WT and  $Rag1^{-/-}$  in naïve and stroke conditions using the Smart-Seq2 platform.** **a** Correlation between the 291 pools of microglia. Hierarchical clustering identified 7 clusters, named from S1 to S7. The amount of samples is in between parentheses. The 1000 most variable genes were considered. The color represents the Pearson correlation coefficient between the samples. **b-d** UMAP plots showing the samples colored by clusters (b), genotype (c) and condition (d) and their associated cell distribution of genotypes and conditions among the sample clusters. **e** Average expression of gene clusters (defined in panel g) within each sample cluster. Scale is the average of the log normalized expression. **f** Box plots of the gene clusters in each conditions and genotypes. Grey boxes highlight significant difference between WT and  $Rag1^{-/-}$  in stroke condition. \*, P < 0.05; \*\*, P < 0.01; \*\*\*, P < 0.001. Non-parametric Kruskal Wallis test followed by multiple non-parametric Wilcoxon t-tests and Bonferroni post-hoc correction for multiple testing. **g** Gene clusters and associated pathway enrichment analysis. Hierarchical clustering identified 7 gene clusters, named G1 to G7, only the significantly regulated gene clusters G1 and G3 between WT and  $Rag1^{-/-}$  in stroke condition are shown. Each barplot shows the pathway enrichment analysis for the genes included in the gene clusters.

144 Next, we aimed to validate our scRNA-seq findings by an independent transcriptomic platform using  
145 Smart-seq2 profiling of sorted pools of 50 microglia which provides cell type specificity and higher  
146 mRNA capture than scRNA-seq (Picelli et al., 2014). We confirmed a predominant effect of stroke on  
147 the microglial transcriptome (**Fig. 2a, b**), in which lymphocyte-deficiency affected the abundance of  
148 specific microglia subsets (**Fig. 2c–e**). In order to identify the pathways specifically regulated in these  
149 subsets, we performed a 'Sample-Gene cluster' correlation analysis and identified two gene sets that  
150 were significantly regulated between WT and  $Rag1^{-/-}$  mice after stroke (i.e., G1 and G3; **Fig. 2f, g**).  
151 Specifically, we detected a decrease of gene expression associated with glial cell migration and  
152 leukocyte differentiation (gene cluster G3), and an increase in neutrophil degranulation and cytokine  
153 production (G1) in lymphocyte-deficient mice (**Fig. 2g**), supporting our results from the single cell  
154 sequencing obtained with the 10x protocol. Altogether, we demonstrated that lymphocytes modulate  
155 the activation status of a subset of stroke-associated microglial cells towards a phenotype associated  
156 with increased phagocytosis and immune cell accumulation in the post-ischemic brain.  
157

### 158 **T<sub>HELPER</sub> cell subpopulations drive the distinct polarization of microglia**

159 To test whether microglial phenotypes can be specifically skewed by functionally opposing T<sub>HELPER</sub> cell  
160 subpopulations, we differentiated T<sub>H1</sub> and regulatory T cells (T<sub>REG</sub>) *in vitro* (Supplementary Fig. 3a) and  
161 tested whether these T<sub>HELPER</sub> cells can reprogram the stroke-associated microglia. Differentiated T cells  
162 or vehicle were injected into the cisterna magna (CM) of lymphocyte-deficient  $Rag1^{-/-}$  mice 24 h after  
163 stroke. Microglia cells were sorted from the ipsilesional hemisphere 24 h after polarized T<sub>HELPER</sub> cell (T<sub>H1</sub>  
164 or T<sub>REG</sub> cells) or vehicle administration (**Fig. 3a**). The transcriptional profile of microglia induced by T<sub>REG</sub>  
165 cells was more similar to vehicle treated  $Rag1^{-/-}$  mice (named control (CT)), than microglial gene  
166 expression induced by T<sub>H1</sub>, as shown in the heatmap and volcano plots of the differentially expressed  
167 genes ( $P < 0.05$  and  $|fold change| > 3$ ) with 51 and 20 microglial genes regulated in T<sub>H1</sub> or T<sub>REG</sub> conditions  
168 compared to control injection, respectively (**Fig. 3b, c**). Gene ontology analysis of the differentially up-  
169 regulated genes revealed T<sub>H1</sub>-dependent pathways associated with antigen presentation, response to  
170 cytokines and regulation of type I interferon whereas T<sub>REG</sub>-dependent microglial genes were associated  
171 with chemotaxis (**Fig. 3d**). These results demonstrate the potency of T cell subpopulations to  
172 differentially skew the microglial transcriptome towards distinct phenotypes previously associated with  
173 different cellular functions. In particular, we found that T<sub>H1</sub> polarized microglia toward an antigen-  
174 immunocompetent phenotype (*Cd74*) and expression of interferon response-related genes (*Irf7*). This  
175 profile of microglial response was previously associated with a pronounced immune response during  
176 the later stages of neurodegeneration (Mathys et al., 2017). In contrast, T<sub>REG</sub> cells promoted the  
177 expression of chemokines/cytokines in microglia (*Ccl2*, *Ccl7*, *Cxcl10*), which can have either pro-  
178 regenerative or detrimental effects such as the regulation of leukocyte chemotaxis to the injured brain  
179 (Llovera et al., 2017), mechanisms of protective preconditioning (Garcia-Bonilla et al., 2014) or  
180 promoting neuronal stem cell recruitment and angiogenesis (Andres et al., 2011; Lee et al., 2012; Liu  
181 et al., 2007). In addition, after experimental stroke, the T<sub>H1</sub>-mediated effects on the microglial  
182 transcriptomic profile were associated with an increase of *Trem2* expression, a key marker of disease-

183 associated microglia in various brain disorders, in comparison to microglia primed by T<sub>REG</sub> cells (Fig.  
 184 3e). These transcriptomic differences in microglia related to the *in vivo* T<sub>H1</sub> or T<sub>REG</sub> cell exposure was  
 185 also reflected by the difference in the morphology of microglia between these conditions. Microglia  
 186 displayed a reactive state as shown by a more spherical and less branched morphology in T<sub>H1</sub> cell-  
 187 injected compared to T<sub>REG</sub>-injected mice (Fig. 3f).

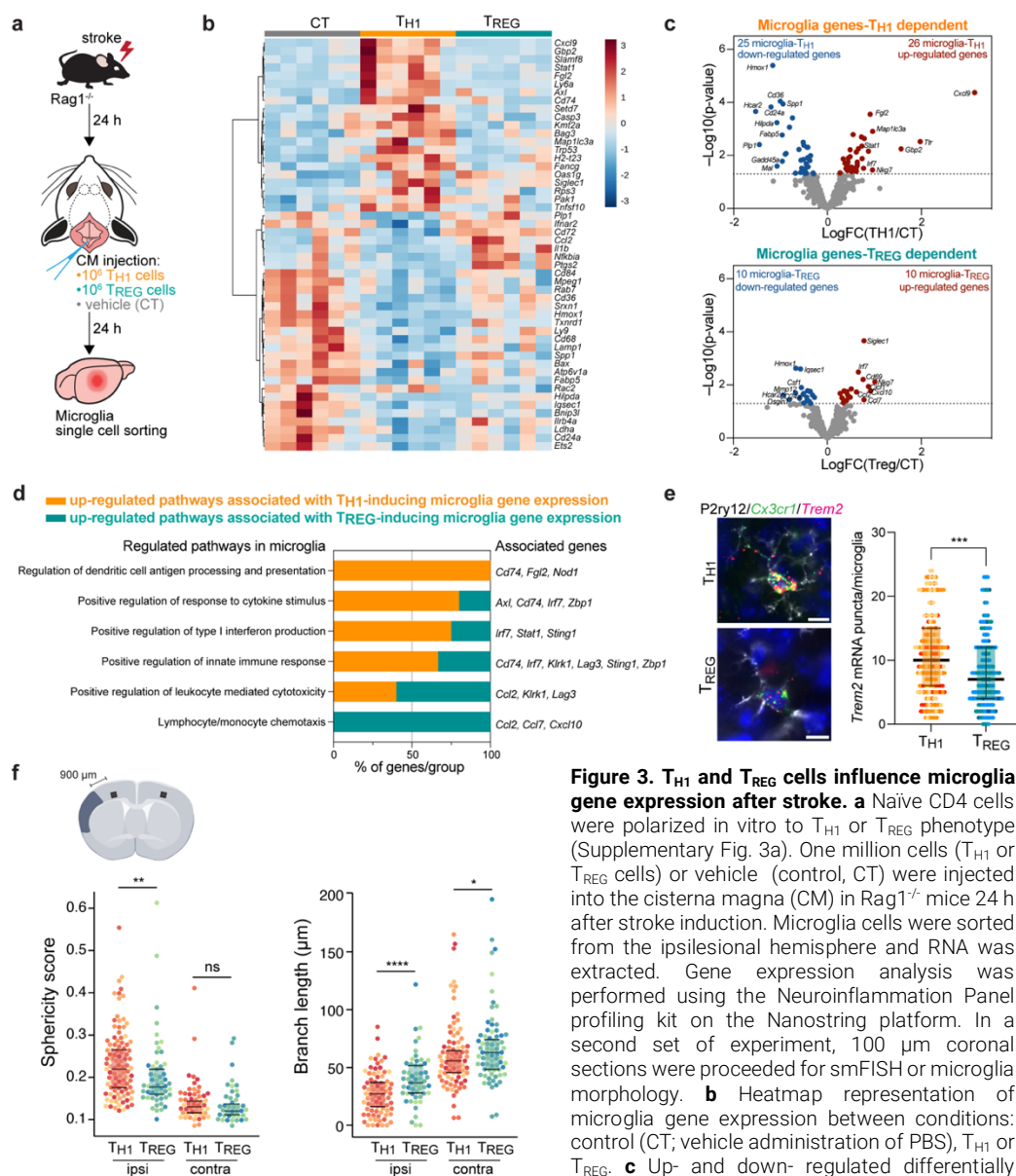


**Figure 3. T<sub>H1</sub> and T<sub>REG</sub> cells influence microglia gene expression after stroke.** **a** Naive CD4 cells were polarized in vitro to T<sub>H1</sub> or T<sub>REG</sub> phenotype (Supplementary Fig. 3a). One million cells (T<sub>H1</sub> or T<sub>REG</sub> cells) or vehicle (control, CT) were injected into the cisterna magna (CM) in Rag1<sup>-/-</sup> mice 24 h after stroke induction. Microglia cells were sorted from the ipsilesional hemisphere and RNA was extracted. Gene expression analysis was performed using the Neuroinflammation Panel profiling kit on the Nanostring platform. In a second set of experiment, 100 μm coronal sections were proceeded for smFISH or microglia morphology. **b** Heatmap representation of microglia gene expression between conditions: control (CT; vehicle administration of PBS), T<sub>H1</sub> or T<sub>REG</sub>. **c** Up- and down- regulated differentially expressed genes between either isolated

microglia from T<sub>H1</sub>- (top) and T<sub>REG</sub>- (bottom) treated Rag1<sup>-/-</sup> mice relative to control condition (microglia isolated from Rag1<sup>-/-</sup> mice treated with vehicle, genes are color-coded accordingly to a p-value < 0.05 and |fold change| > 3). **d** Pathway analysis was performed for the up-regulated genes in each condition using the ClueGO package from Cytoscape. **e** Higher amount of Trem2 mRNA puncta (red) per Cx3cr1-positive (green) in P2ry12-labelled microglia (white) in T<sub>H1</sub>-treated mice in comparison the T<sub>REG</sub>-treated mice. DAPI (blue) was used as nuclear dye. Scale bar = 10 μm. **f** Morphological analysis of IBA1+ microglia in the ipsilateral (900 μm distal to the infarct border, cortical layer 4) and contralateral hemisphere, as shown in the representative coronal section. Sphericity score and branch length (μm) of microglia treated with T<sub>H1</sub> (orange) or T<sub>REG</sub> cells (green). Each individual mouse is represented in the plots by one color (3 mice/condition), each dot corresponds to one microglial cells; ns, non significant; \*, P < 0.05; \*\*, P < 0.01; \*\*\*\*, P < 0.0001. Wilcoxon rank sum test with continuity correction and Bonferroni post-hoc correction for multiple testing.

190 Interestingly, these morphological changes were not only restricted to the ipsilesional hemisphere but  
191 were also observed in the contralateral hemisphere, suggesting possible brain-wide effects of  
192 differentiated T<sub>HELPER</sub> cells injected to the cerebrospinal fluid (CSF) compartment. In accordance, we  
193 found that intra-CM injection of eGFP-labelled T<sub>H1</sub> cells to Rag1<sup>-/-</sup> mice after stroke were primarily  
194 recruited to the ischemic brain parenchyma, but were additionally also localized in border tissues  
195 including the meninges, and some CM-injected cells even circulated and could be detected in the  
196 spleen. (Fig. 4a, b and Supplementary Fig. 3b). Together, these findings support that polarized T cells  
197 are recruited to the infarction site and may modify *in situ* the inflammatory micromilieu.

198

### 199 **Engineered T cells overexpressing IL-10 induce a pro-regenerative microglial phenotype**

200 In order to further explore the therapeutic potential of T cell-secreted cytokines to modulate the local  
201 microglial immune milieu, we engineered T cells by viral transfection to overexpress the anti-  
202 inflammatory cytokine IL-10 (eTc-IL10; Supplementary Fig. 3c,d). In a therapeutic approach, we injected  
203 eTc-IL10 cells into the CM of WT mice 4 h after stroke – a translationally relevant time window  
204 considering a similar time window for acute therapy with thrombolytics in stroke patients. We  
205 investigated whether eTc-IL10 treatment affected stroke outcome but did not find any difference in  
206 infarct volumes between conditions (Fig. 4c). This is in accordance with the concept of early ischemic  
207 lesion formation in stroke which is not being affected by the delayed immunological mechanisms  
208 (Dirnagl et al., 1999). In contrast, mice receiving eTc-IL10 injection in the CM had a substantially  
209 improved functional outcome at 48 h after stroke as shown by a reduced forelimb assymetry (Fig. 4d).  
210 This might reflect the particular impact of inflammatory pathways and specifically cytokine secretion  
211 on functional deficits and delayed recovery after stroke in contrast to the early primary lesion  
212 development (Filiano et al., 2017; Roth et al., 2020). We then evaluated whether gene expression was  
213 altered after stroke upon eTc-IL10 treatment. RNA was isolated from the whole ischemic hemisphere  
214 and neuroinflammatory genes were quantified using the Nanostring platform. Interestingly, we found  
215 that several genes associated with a disease-associated microglial profile were down-regulated in mice  
216 treated with eTc-IL10 such as *CD68*, *Apoe*, *Itgax*, *Trem2*, *Tyrobp* and *Cst7* (Fig. 4e and Supplementary  
217 Fig. 3e). Gene ontology analysis revealed that T cell-derived IL-10 overexpression increased pathways  
218 associated with chemokine responses, and the downregulation of several microglial effector functions  
219 such as spine pruning, phagocytosis and complement activation (Fig. 4f). This anti-inflammatory effect  
220 of eTc-IL10 treatment on microglia was confirmed by a reduction of *Trem2* mRNA in *Cx3cr1*<sup>+</sup> microglia  
221 from eTc-IL10 compared to vehicle-treated mice (Fig. 4g). Since we observed a down regulation of  
222 genes associated with synapse pruning (*C1qa*, *C1qc*), microglia activation (*P2ry12*, *Cx3cr1*) and  
223 phagocytosis (*Trem2*) in mice treated with eTc-IL10, we postulate that acute intra-CM administration  
224 of eTc-IL10 induces a switch of genes characteristic of homeostatic microglia possibly promoting post-  
225 stroke recovery mechanisms.

226

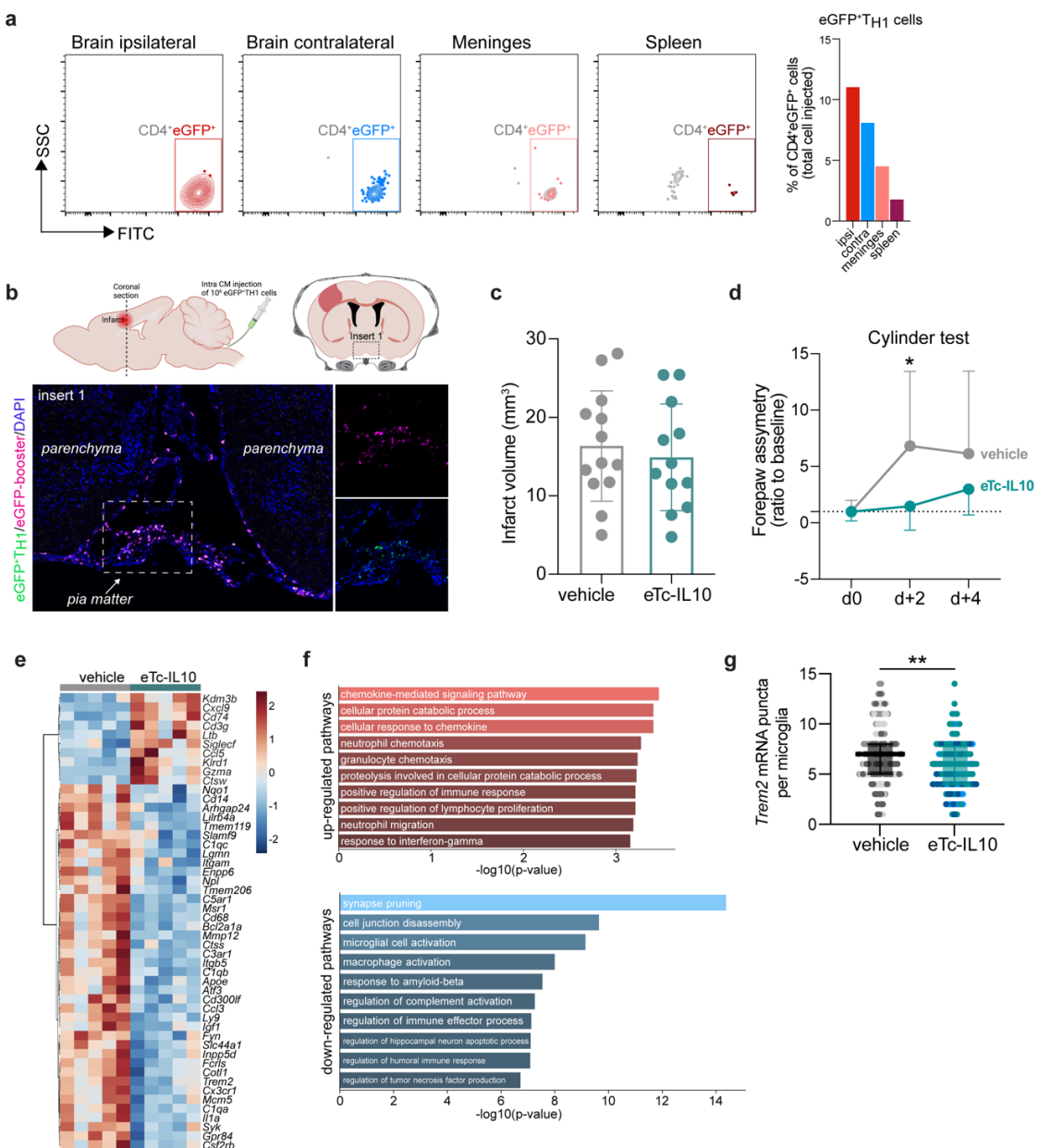


**Figure 4. Acute post-stroke treatment with engineered T cells overexpressing IL-10 modulates microglial activation and ameliorates functional deficit.** **a, b** Flow cytometry analysis and whole skull-brain coronal sections of 10<sup>6</sup> eGFP+T<sub>H1</sub> cells injected into the cisterna magna (CM) of Rag1<sup>-/-</sup> mice 24 h after stroke. Samples were collected 4 h after CM injection for further analysis: **a** Flow cytometry plots showing CD4<sup>+</sup>eGFP<sup>+</sup> cells isolated from the brain (ipsilateral and contralateral hemispheres), meninges and spleen (the detailed gating strategy is shown in Supplementary Fig. 3b). The graph represents the percentage of eGFP+T<sub>H1</sub> cells relative to the total number of cells injected in the CM (10<sup>6</sup> eGFP+T<sub>H1</sub> cells). **b** Coronal section showing eGFP+T<sub>H1</sub> cells in the meninges. Insert 1 indicates a representative photomicrograph of eGFP+T<sub>H1</sub> cells counterstained with an eGFP-booster (magenta), cell nuclei are stained with DAPI (blue). The magnified images of white boxed area show eGFP+T<sub>H1</sub> cells injected into the CM are located in the meninges. **c** Infarct volumes at 5 d after stroke in WT C57BL/6J mice treated by CM administration of either T cells secreting IL-10 (eTc-IL10, 10<sup>6</sup> naïve CD4+ cells transfected with a plasmid overexpressing IL-10, Supplementary Fig. 3c, d) or vehicle (aCSF) 4 h after stroke induction. **d** Percentage of assymetry in independent forepaw use ("0%" indicates symmetry) in mice treated with vehicle or eTc-IL10; \*, P < 0.05, ANOVA with Šidák's multiple comparisons test. **e** Heatmap representation of ipsilateral brain gene expression between vehicle and eTc-IL10 treated mice 5 d after stroke. **f** Selected gene ontology annotations for the 50 genes that were up-regulated (top) and down-regulated (bottom) in the whole ipsilateral brain tissue of eTc-IL10 treated mice in comparison to vehicle treated mice. **g** smFISH analysis of brains from eTc-IL10 treated mice showed a reduction of Trem2 mRNA puncta per Cx3cr1<sup>+</sup> microglia in the peri-infarct region in comparison to vehicle treated mice; \*\*, P < 0.01, Mann-Whitney U test.

229 **Discussion**

230 The cellular constituents of the acute neuroinflammatory response to stroke has been well  
231 characterized including microglial activation, leukocyte invasion and the contribution of different  
232 lymphocyte subpopulation (Anrather and Iadecola, 2016). However, the reciprocal interactions of these  
233 different immune cell populations remain largely underinvestigated in the context of brain injury. A  
234 better understanding of the T cell polarizing effect on microglial function has strong translational  
235 implication, since T cells may act as a 'Trojan horse' with large impact on the cerebral inflammatory  
236 milieu potentiated by microglia (Cramer et al., 2018).

237

238 Here, we established a mechanistic link between T cells and microglial function and showed the distinct  
239 role of T cell subpopulations on switching microglial polarization state in response to stroke. Our results  
240 from transcriptomic analysis suggest that the microglia-polarizing effect of different  $T_{\text{HELPER}}$  cell  
241 subpopulations is mainly mediated via their specific cytokine secretion pattern. Microglia that were  
242 challenged with  $T_{\text{H1}}$  cells expressed an upregulation of genes associated with type I interferon signaling  
243 (INF) – the key cytokine secreted by the  $T_{\text{H1}}$  subpopulation. In contrast,  $T_{\text{REG}}$  cells modulated a gene set  
244 associated with chemotaxis-mediated mechanisms and downregulated activation markers such as the  
245 expression of *Trem2*, which have previously been described to be regulated by the  $T_{\text{REG}}$ -cytokine IL-10  
246 (Shemer et al., 2020). These previous and our own results here clearly show the direct role of IL-10 in  
247 modulating microglial function. Likewise, using adult human microglial cells co-culture with T  
248 lymphocytes others demonstrated an enrichment of IL-10 secretion upon direct cell-cell contact  
249 (Chabot et al., 1999). In addition, we previously reported using whole genome sequencing that  
250 intracerebroventricular injection of IL-10 is sufficient to modulate the neuroinflammatory response  
251 after experimental stroke (Liesz et al., 2014).

252

253 An important caveat and potential key reason for the so far still pending success in harnessing the  
254 therapeutic function of IL-10 is its short half-life (less than 1 hour) and limited bioactivity after *in vivo*  
255 administration as a recombinant protein (Le et al., 1997; Saxena et al., 2015). Moreover, the systemic  
256 IL-10 application can have considerable and unforeseen side-effects due to the potentially divergent  
257 function of IL-10 on inflamed and homeostatic tissue, including direct effects on neurons, astrocytes,  
258 endothelial cells and other cellular constituents of physiological brain function (Saraiva et al., 2019).  
259 Therefore, we aimed to take a different approach for the localized and sustained production of IL-10 at  
260 the inflamed peri-lesional brain parenchyma. For this we took advantage of the potent capability of T  
261 cells to be specifically recruited and accumulated to the ischemic lesion site in order to deliver IL-10  
262 from genetically engineered IL-10-overexpressing T cells (Heindl et al., 2021; Llovera et al., 2017). We  
263 demonstrated that IL-10 overexpression by this approach substantially modulated microglia function  
264 by down-regulation of microglial gene signature associated with phagocytosis of synapses correlating  
265 with functional recovery after stroke. Interestingly, eTc-IL10 cells did not exclusively invade the injured  
266 brain, but were also located in the meningeal compartment and could additionally contribute to  
267 functional recovery by resolving inflammation at these broader structures or providing IL-10 to the brain

268 parenchyma along CSF flow. This concept is in accordance with previous observations of meningeal  
269 immune cell accumulation after stroke (Benakis et al., 2018) and that meningeal T cell-derived  
270 cytokines may enter the brain via CSF flow and paravascular spaces (Iliff et al., 2012).  
271 An important finding in this study was the observation that IL-10 overexpression in T cells modulated  
272 microglial genes involved in the complement pathway, phagocytosis and synaptic pruning, and was  
273 associated with a better functional outcome after stroke. Complement factors are localized to  
274 developing CNS synapses during periods of active synapse elimination and are required for normal  
275 brain wiring (Schafer et al., 2012). Inactive synapses tagged with complement proteins such as C1q  
276 may be eliminated by microglial cells. Likewise in the mature brain, early synapse loss is a hallmark of  
277 several neurodegenerative diseases (Stephan et al., 2012). Indeed, complement proteins are profoundly  
278 upregulated in many CNS diseases prior to signs of neuron loss, suggesting mechanisms of  
279 complement-mediated synapse elimination regulated by microglia potentially driving disease  
280 progression (Stephan et al., 2012) and stroke recovery. It is therefore conceivable that T cells  
281 overexpressing IL-10 down-regulate the complement system in microglia and prevent excessive  
282 elimination of synapse and consequently protect against neuronal dysfunction. This is particularly of  
283 interest because microglia effector function have not only been associated with inflammatory  
284 neurodegenerative processes, but recently also been shown to be neuroprotective (Szalay et al., 2016)  
285 by tightly monitoring neuronal status through somatic junctions (Cserép et al., 2020). Microglia interact  
286 with the extra-neuronal space by not only regulating the elimination of existing synapses but also by  
287 modifying the extracellular matrix to enable efficient synaptic remodelling (Zaki and Cai, 2020).  
288 Accordingly, we found T cell-dependent regulation of several microglial genes that can mediate such  
289 extracellular matrix modifications involved in phagocytosis and proteases (*Clstn1* and *Mmp12*,  
290 cathepsins and MMPs, respectively).  
291  
292 Taken together, we have been able to demonstrate that brain-invading T cells can specifically "fine-  
293 tune" the transition of microglial to a reactive state. We postulate that the development of engineered  
294 T cells could have important translational implication by targeting a specific effector function of  
295 microglia with a relevant impact on the chronic progression of stroke pathobiology.  
296

297 **Materials and Methods**

298 **Animal experiments**

299 All animal procedures were performed in accordance with the guidelines for the use of experimental  
300 animals and were approved by the respective governmental committees (Regierungspraesidium  
301 Oberbayern, the Rhineland Palatinate Landesuntersuchungsamt Koblenz). Wild-type C57BL6/J mice  
302 were purchased from Charles River, Rag-1<sup>-/-</sup> mice (NOD.129S7(B6)-Rag-1tm1Mom/J) and eGFP-  
303 reporter mice (C57BL/6-Tg(CAG-EGFP)131Osb/LeySopJ) were bred and housed at the animal core  
304 facility of the Center for Stroke and Dementia Research (Munich, Germany). All mice were housed with  
305 free access to food and water at a 12 h dark-light cycle. Data were excluded from all mice that died  
306 during surgery. Animals were randomly assigned to treatment groups and all analyses were performed  
307 by investigators blinded to group allocation. All animal experiments were performed and reported in  
308 accordance with the ARRIVE guidelines (Kilkenny et al., 2011).

309

310 **Permanent distal middle cerebral artery occlusion model**

311 Permanent coagulation of the middle cerebral artery (MCA) was performed as previously described  
312 (Llovera et al., 2014). Briefly, animals were anesthetized with volatile anesthesia (isofurane in  
313 30%O<sub>2</sub>/70%N<sub>2</sub>O) and placed in lateral position. After a skin incision between eye and ear, the temporal  
314 muscle was removed and the MCA identified. Then, a burr hole was drilled over the MCA and the dura  
315 mater was removed. The MCA was permanently occluded using bipolar electrocoagulation forceps.  
316 Permanent occlusion of the MCA was visually verified before suturing the wound. During the surgery,  
317 body temperature was maintained using a feedback-controlled heating pad. Mice that developed a  
318 subarachnoid hemorrhage during surgery were excluded from the analysis.

319

320 **Cylinder test**

321 To evaluate forepaw use and asymmetry, the cylinder test was performed two days prior to stroke  
322 (baseline) and day 2 and day 4 post stroke. Mice were placed in a transparent acrylic glass cylinder  
323 (diameter 8cm; height: 25 cm) in front of two mirrors and videotaped. To assess independent forelimb  
324 use, contact with one forelimb (left and right forelimbs) during full rearing and landing performance of  
325 mice were scored by frame-to-frame analysis of recorded videos. Mice with forepaw preference at  
326 baseline (absolute value difference between right and left forepaws > 10) were excluded from the  
327 analysis. All rearing movements during the trial were counted and used as indication of the animal's  
328 overall activity.

329

330 **Intra cisterna magna injection**

331 Mice were anesthetized with isofurane in 30%O<sub>2</sub>/70%N<sub>2</sub>O and fixed in a stereotaxic frame by the  
332 zygomatic arch, with the head slightly tilted to form an angle of 120° in relation to the body. A small  
333 incision was made at the nape of the neck between the ears to expose the neck muscles, which were  
334 bluntly dissected to expose the cisterna magna (CM). Cannulas composed of a glass capillary (ID, inner  
335 diameter 0.67 mm; OD, outside diameter, 1.20 mm) attached to a polyethylene tubing (ID 0.86 mm, OD

336 1.52mm, Fisher Scientific UK Ltd.) were used to perform the CM injections. Glass capillaries were  
337 sharpened using a flaming micropipette puller (P-1000, Sutter Instrument GmbH), filled with 10  $\mu$ l of the  
338 cell suspension diluted in artificial CSF (aCSF: 126 mM NaCl, 2.5 mM KCl, 1.25 mM NaH<sub>2</sub>PO<sub>4</sub>, 2 mM  
339 Mg<sub>2</sub>SO<sub>4</sub>, 2 mM CaCl<sub>2</sub>, 10 mM glucose, 26 mM NaHCO<sub>3</sub>; pH 7.4 when gassed with 95% O<sub>2</sub> and 5% CO<sub>2</sub>)  
340 and fixed to the micromanipulator arm of the stereotaxic. Cell suspension was injected into the CM at  
341 a rate of 2  $\mu$ l/min. At the end of the injection mice are sutured and allowed to recover in a preheated  
342 awake cage for 1 h, after which they are returned to the animal husbandry.

343

#### 344 **Infarct volume quantification**

345 Mice were deeply anesthetized 5 days after stroke induction and transcardially perfused with 20 ml  
346 saline. Brains were removed, frozen immediately on powdered dry ice and stored at -20 °C until use.  
347 For infarct volumetry, brains were serially sectioned (400  $\mu$ m intervals, 20  $\mu$ m thick) and stained for  
348 cresyl violet (CV) as previously described (Llovera et al., 2014). CV stained sections were scanned at  
349 600 dpi on a flatbed scanner (Canon). Direct infarct measurement was used after validating the absence  
350 of edema at the investigated time point. The total infarct volume was measured with ImageJ and  
351 determined by integrating measured areas and distances between sections.

352

#### 353 **Immunohistochemistry and confocal microscopy**

354 Microglia morphology analysis was performed on brain coronal sections as previously described  
355 (Heindl et al., 2018). Briefly, mice were perfused with 4% paraformaldehyde (PFA) and brains were post-  
356 fixed overnight and placed in sucrose for dehydration. Then, free floating 100  $\mu$ m coronal sections were  
357 stained for microglia with 1:200 anti-Iba1 (rabbit, Wako, #019-19741). Nuclei were stained using 4',6-  
358 Diamidin-2-phenylindol (DAPI, Invitrogen, #D1306) and images were acquired at a distance of 900  $\mu$ m  
359 from the border of the lesion in layer 4 (ipsilateral) and the homotypic contralateral region using a Zeiss  
360 confocal microscope with 40x magnification (objective: EC Plan-Neofluar 40x/1.30 Oil DIC M27) with  
361 an image size of 1024  $\times$  1024 pixel, a pixel scaling of 0.2  $\times$  0.2  $\mu$ m and a depth of 8 bit. Confocal-images  
362 were collected in Z-stacks with a slice-distance of 0.4  $\mu$ m. Morphological features of microglia were  
363 acquired using a fully automated analysis as previously described (Heindl et al., 2018).

364

#### 365 **Fluorescent In Situ Hybridization (FISH)**

366 Single-molecule fluorescence in situ hybridization (FISH) was performed using the RNAscope Multiplex  
367 Fluorescent Reagent Kit v2 (Advanced Cell Diagnostics) by the manufacturer's protocols. Briefly, free  
368 floating 100  $\mu$ m coronal brain sections (Fig. 3e) or 20  $\mu$ m cryo-sections (Fig. 4g) were first dried,  
369 washed, and then incubated in RNAscope hydrogen peroxide. Antigen retrieval and protease treatment  
370 were performed as per protocol. Sections were then incubated with the probe mix (C2-Trem2 and C1-  
371 Cx3cr1) for 2 h at 40°C and then immediately washed with wash buffer. Next, sections were incubated  
372 with RNAscope Multiplex FL v2 AMP1, AMP2, and AMP3, and then probes were counterstained with  
373 TSA Plus Cy3 for C1-Cx3cr1, TSA Plus Cy5 for C2-Trem2. For microglia identification (Fig. 3e), slides  
374 were incubated in blocking at RT for 1 h before overnight incubation at 4°C with the primary rabbit anti-

375 P2Y12 receptor antibody (1:200, AnaSpec #AS-55043A) and labelling for 1 hour with the secondary  
376 antibody AF488 goat anti-rabbit, (1:200, Invitrogen #A11034). Finally, sections were stained with DAPI  
377 (Invitrogen) and mounted with fluoromount medium (Sigma). smFISH-stained RNA molecules were  
378 counted only within the DAPI staining of the cell; a cell was considered *Cx3cr1*-positive when more than  
379 four *Cx3cr1* puncta were present.

380

### 381 **Whole skull immunofluorescence**

382 *Rag1<sup>-/-</sup>* mice were anesthetized with isoflurane and perfused transcardially with ice-cold PBS followed  
383 by 4% PFA. After removing the mandibles, skin and muscles were carefully detached from the skull  
384 (<http://www.nature.com/protocolexchange/protocols/3389>). The skull decalcification was performed  
385 as previously described (Benakis et al., 2016). Coronal skull sections (20 µm) were stained with GFP-  
386 booster Atto647N (1:500, ChromoTek GmbH) to visualize eGFP-labelled T cells. Sections were  
387 counterstained with DAPI (Invitrogen) to visualize cell nuclei and observed by confocal laser  
388 microscopy (Leica SP5).

389

### 390 **In vitro T cell polarization**

391 Single-cell suspensions were generated from spleen, inguinal, axial, brachial, and mandibular lymph  
392 nodes of C57BL/6 or b-actin-EGFP mice by passing the tissue through a 70-µm cell strainer. Naive CD4+  
393 T cells were obtained by pre-enrichment using an “untouched” CD4+ T Cell Isolation Kit (Miltenyi Biotec)  
394 with subsequent flow cytometric analysis (CD4+ [clone RM4-5, 0.5 ng/µL], CD44low [clone IM7, 2  
395 ng/µL], CD62Lhigh [MEL-14, 0.8 ng/µL]). Cells were seeded at a density of 300,000 or 400,000 cells/  
396 well in a flat-bottom 96-well plate and stimulated with plate-bound anti-CD3 and anti-CD28 Abs (0.5  
397 µg/mL or 2 µg/mL anti-CD3 [clone 145-2C11] for  $T_{REG}$  and  $T_{H1}$ , respectively and 2 µg/mL anti-CD28  
398 [clone 37.51]. Different mixtures of cytokines and mAbs were added to RPMI (supplemented with 10%  
399 FCS, 50 µM  $\beta$ -mercaptoethanol, 50 U/mL penicillin, 50 µg/mL streptomycin, 1% GlutaMAX™ and 1% N-  
400 2-hydroxyethylpiperazine-N-2-ethane sulfonic acid [Gibco® HEPES]) and used as follow:  $T_{H1}$  conditions  
401 with anti-IL-4 (10 µg/mL, BioXCell, #BE0045) and IL-12 (10 ng/mL, BioLegend, #577002);  $T_{REG}$   
402 conditions: anti-IL-4 (10 µg/mL, BioXCell, #BE0045), anti-IFN- $\gamma$  (10 µg/mL, BioXCell, #BE0055) and  
403 TGF $\beta$  (3ng/mL, BioLegend, #580702). After 2 days in culture, cells were split into 2 new 96-well plates  
404 and incubated with freshly prepared supplemented RPMI media with IL-2 (10 ng/ml, BioLegend,  
405 #575402). Cells were cultured for a total of 5 days before injection. Quality control was performed on  
406 day 4 to assess the percentage of T cell expressing Tbet (clone 4B10, 2 ng/µL) ( $T_{H1}$ ) or FoxP3 (clone  
407 FJK-16s, 2 ng/µL) ( $T_{REG}$ ) (Supplemental Fig. 3a). One million differentiated T cells were resuspended in  
408 sterile aCSF and injected into the CM in *Rag1<sup>-/-</sup>* recipient mice 24 h after dMCAO induction.

409

### 410 **IL-10 overexpression in naïve T cells**

411 Engineered T cells overexpressing IL-10 (eTc-IL10) were generated by transfection of naïve T cells with  
412 an IL-10 plasmid (pRP[Exp]-TagBFP2-CMV>mIL10[NM\_010548.2]) designed and prepared by  
413 VectorBuilder (Supplementary Fig. 3c). First, splenocytes were isolated from C57BL/6 mice (male, 6-12

414 weeks old) and enriched using a CD4+ T Cell Isolation Kit (Miltenyi Biotec, No:130-104-453). Quality  
415 control was performed by flow cytometry (CD4+ [clone RM4-5, 1:25], CD44low [clone IM7, 1:25],  
416 CD62Lhigh [clone MEL-14, 1:25]). Cells were resuspended in RPMI (supplemented with 10% FBS, 50  $\mu$ M  
417  $\beta$ -mercaptoethanol, 50 U/mL penicillin, 50  $\mu$ g/mL streptomycin, 1% GlutaMAX, 1% HEPES and 10 ng/mL  
418 IL-2). To induce CD4+ cells to enter the cell cycle for efficient DNA uptake,  $4 \times 10^5$  cells/well were seeded  
419 in a flat-bottom 96-well plate containing bound anti-CD3 (2  $\mu$ g/mL, clone 145-2C11) and anti-CD28 (2  
420  $\mu$ g/mL, clone 37.51) for 48 h. After 48 h stimulation,  $1.5 \times 10^6$  cells multiplied by the number of mice to  
421 be injected were transfected with the pIL-10 vector ( $1 \times 10^6$  cells/1.5  $\mu$ g pIL-10 DNA per cuvette) using  
422 the Mouse T Cell Nucleofector Kit (Lonza, No: VPA-1006) with Nucleofector II Device (program X-100).  
423 Once electroporated, cells were diluted with conditioned RPMI from the 48 h stimulation and fresh  
424 supplemented RPMI (1:1) and seeded in a 12-well plate (1 cuvette of cells/ well). 24 h post transfection,  
425 cells and supernatant were collected. Supernatant was used to confirm IL-10 secretion by ELISA  
426 (Supplementary Fig. 3c) and cells were collected for intra CM injection ( $1 \times 10^6$ /mouse).

427

#### 428 **ELISA**

429 Secreted IL-10 was determined by ELISA as per the manufacturer's protocol (Mouse IL-10, Invitrogen,  
430 No: 88-7105-88). The color reaction was measured as OD450 units on a Bio-Rad iMark microplate  
431 reader. The concentration of supernatant IL-10 was determined using the manufacturer's standard  
432 curve over the range of 32-4'000 pg/mL.

433

#### 434 **Flow cytometry**

435 For differentiation of live and dead cells we stained cells with the Zombie Violet Fixable Viability Kit  
436 according to the manufacturer's instructions (BioLegend). For surface marker analysis, cell  
437 suspensions were adjusted to a density of  $0.5 \times 10^6$  cells in 50  $\mu$ l FACS buffer (2% FBS, 0.05%  $\text{NaN}_3$  in  
438 PBS). Nonspecific binding was blocked by incubation for 10 min at 4 °C with anti-CD16/CD32 antibody  
439 (Biolegend, clone 93, 5 ng/  $\mu$ L) antibody and stained with the appropriate antibodies for 15 min at 4 °C.  
440 The following antibodies were used for extracellular staining: CD45 (clone 30F-11, 0.5 ng/ $\mu$ L), CD4  
441 (clone RM4-5, 0.5 ng/ $\mu$ L), CD11b (clone M1/70, 0.6 ng/ $\mu$ L), CD19 (eBio1D3, 0.6 ng/ $\mu$ L), B220 (clone  
442 RA3-6B2, 0.32 ng/ $\mu$ L), CD3 $\epsilon$  (clone 145-2C11, 2 ng/ $\mu$ L), CD8a (clone 53-6.7, 2 ng/ $\mu$ L), CD62L (clone  
443 MEL-14, 0.8ng/ $\mu$ L) from ThermoFisher. For intracellular cytokine staining, cells were restimulated for 4  
444 hours with PMA (50ng/ml, Sigma), ionomycin (1  $\mu$ M, Sigma) and brefeldin A (1  $\mu$ l for  $\sim 10^6$  cells/mL).  
445 Cells were then stained for surface markers as detailed below, fixed and permeabilized using Fixation  
446 and Permeabilization Buffers from eBiosciences following the manufacturer's instructions. Briefly, cells  
447 were fixed for 30 min at 4 °C (or RT for FoxP3), washed with permeabilization buffer and incubated for  
448 30 min with the appropriate antibodies in permeabilization buffer at 4 °C (or RT for FoxP3). The cells  
449 were stained with the transcription factors FoxP3 (clone FJK-16s, 2 ng/ $\mu$ L) and T-bet (clone 4B10, 2  
450 ng/ $\mu$ L) or IFN- $\gamma$  (clone 4S.B3, 2 ng/ $\mu$ L). Cells were washed with FACS buffer, resuspended in 200  $\mu$ l of  
451 FACS buffer and acquired using a BD FACSVerse flow cytometer (BD Biosciences, Germany) and

452 analyzed using FlowJo software (Treestar, US). Isotype controls were used to establish compensation  
453 and gating parameters.

454

#### 455 **Nanostring analysis**

456 The ipsilateral hemispheres were lysed in Qiazol Lysis Reagent and total RNA was extracted using the  
457 MaXtract High Density kit with further purification using the RNeasy Mini Kit (all Qiagen). 70 ng of total  
458 RNA per sample was then hybridized with reporter and capture probes for nCounter Gene Expression  
459 code sets (Mouse Neuroinflammation codeset) according to the manufacturer's instructions  
460 (NanoString Technologies). Samples (6/condition) were injected into NanoString cartridge and  
461 measurement run was performed according to nCounter SPRINT protocol. Background (negative  
462 control) was quantified by code set intrinsic molecular color-coded barcodes lacking the RNA linkage.  
463 As positive control code set intrinsic control RNAs were used at increasing concentrations. Genes  
464 below the maximal values of the negative controls were excluded from the analysis. All gene counts  
465 were normalized (by median) and scaled (mean-centered and divided by standard deviation of each  
466 variable). Heatmaps were performed using the MetaboAnalystR package on normalized expression  
467 values. The regulated genes in microglia treated with  $T_{H1}$  or  $T_{REG}$  in comparison to vehicle treated  
468 microglia (CT) are represented in the volcano plots, genes with a  $P < 0.05$  were color-coded.  
469 Significantly up- regulated genes with a  $FC > 3$  which were specific to  $T_{H1}$  or  $T_{REG}$  (Venn diagram) were  
470 further used for pathway analysis using Cytoscape ClueGO ( $T_{H1}/CT$ : 21 out of 26 genes,  $T_{REG}/CT$ : 5 out  
471 of 10 genes (Bindea et al., 2009)).

472

#### 473 **Microglia cell isolation for RNA sequencing**

474 Mice were perfused transcardially with ice-cold saline containing Heparin (2U/mL). Brains were placed  
475 in HBSS (w/ divalent cations  $Ca^{2+}$  and  $Mg^{2+}$ ) supplemented with actinomycin D (1:1000, 1 mg/mL,  
476 Sigma, #A1410), and microglia was isolated with the Papain-based Neural Tissue Dissociation Kit (P)  
477 (# 130-092-628, Miltenyi Biotec B.V. & Co. KG) according to the manufacturer's instructions. Cell  
478 suspension was enriched using 30% isotonic Percoll gradient.  $1 \times 10^3$ - $1.5 \times 10^3$  live microglia cells from 3  
479 mice per condition were sorted according to their surface marker  $CD45+CD11b+7\text{-AAD}$  negative  
480 (SH800S Cell Sorter, Sony Biotechnology) and proceed for 10x Genomics according to the  
481 manufacturer's instructions (ChromiumTM Single Cell 3' Reagent kits v2). For the Smart-seq2 platform,  
482 pools of 50 cells were sorted into 96 well plates, already filled with 4  $\mu$ L lysis buffer containing 0.05%  
483 Triton X-100 (Sigma) and, ERCC (External RNA Controls Consortium) RNA spike-in Mix (Ambion, Life  
484 Technologies) (1:24000000 dilution), 2.5  $\mu$ M oligo-dT, 2.5 mM dNTP and 2 U/ $\mu$ L of recombinant RNase  
485 inhibitor (Clontech) then spun down and frozen at  $-80^{\circ}\text{C}$ .

486

#### 487 **Single cell data analysis**

488 The CellRanger software (v2.0.0, 10X Genomics) was used for demultiplexing of binary base call (BCL)  
489 files, read alignment, and filtering and counting of barcodes and unique molecular identifiers (UMI).  
490 Reads were mapped to the mouse genome assembly reference from Ensembl (mm10/GRCm38).

491 Downstream data analyses were performed using the Scanpy API (scanpy v>=1.4 with python3 v>=3.5;  
492 (Wolf et al., 2018)). Details on analyses, selected thresholds and package versions are provided in  
493 available source scripts (See Code and Data availability). Outlier and low-quality cells were filtered if  
494 the fraction of mitochondria-encoded counts was greater than 10% or the total number of counts was  
495 greater than 48'000. Thresholds were selected upon visual inspection of distributions as recommended  
496 (Luecken and Theis, 2019). Genes expressed in less than 10 cells were excluded. Further, doublet cells  
497 as identified by the Scrublet algorithm (v0.2.1; (Wolock et al., 2019)) were excluded. Doublet scores and  
498 thresholds were determined for each sample separately. Raw counts of a cell were normalized by total  
499 counts neglecting highly expressed genes which constitute more than 5% of total counts in that cell.  
500 Then, counts were log-transformed ( $\log(\text{count}+1)$ ). These processed and normalized count matrices  
501 were used as input for all further analyses.

502  
503 For the full data set and the microglia subset first a single-cell nearest-neighbor graph was computed  
504 on the first 50 independent principal components. Principle components were calculated using the  
505 3000 most variable genes of the full data set as input. The UMAP algorithm (Becht et al., 2019) as used  
506 to obtain a two-dimensional embedding for visualization. Iterative clustering was performed with the  
507 Louvain algorithm (Blondel et al., 2008) as implemented in louvain-igraph (v0.6.1  
508 <https://github.com/vtraag/louvain-igraph>) with a varying resolution parameter. Clusters were  
509 annotated using previously described marker genes and merged if expressing the same set of marker  
510 genes.

511  
512 Trajectories from homeostatic to reactive microglia were inferred with partition-based graph  
513 abstraction (PAGA) (Wolf et al., 2018) and diffusion pseudotime (DPT) (Haghverdi et al., 2016)  
514 algorithms. First, clusters were grouped into two paths connecting the root and end cell cluster based  
515 on the computed cluster connectivities (PAGA), then, cells were ordered along these paths based on  
516 the random-walk based cell-to-cell distance (DPT). To capture processes specific to the path 2  
517 trajectory in stroke-associated microglia, data was first subset to cells of path 2 and end cells clusters  
518 of stroke samples and gene expressed in less than 20 cells of the subset excluded. Then, gene sets  
519 were computed by clustering the 500 most varying genes using their pairwise-pearson correlation  
520 values as input and Ward's hierarchical clustering method with euclidean distance (scipy python  
521 package v.1.5.4 (Virtanen et al., 2020)). One gene set with average correlation < 0.05 was excluded.  
522 Finally, to obtain an activation score per cell for a given gene set, cell scores were computed as  
523 described by (Satija et al., 2015) and implemented in Scanpy in the *tl.score\_genes* functionality.  
524 Differential activation of gene sets between WT and Rag1<sup>-/-</sup> samples was determined by a Wilcoxon  
525 rank-sum test. To identify genes differentially regulated along the inferred cellular trajectory a  
526 differential gene expression test (Welch t-test with overestimated variance) between the root and end  
527 cell cluster was performed for WT and Rag1<sup>-/-</sup> samples separately. Non-overlapping, significantly  
528 changing genes (p-value <0.05 corrected for multiple testing with the Benjamin-Hochberg method) were  
529 considered as regulated specifically in WT and Rag1<sup>-/-</sup> samples, respectively. Pathway enrichment of

530 gene sets and differentially regulated genes was performed with the gseapy package  
531 (<https://github.com/zqfang/GSEAp/>) functionality of EnrichR (Xie et al., 2021).

532

### 533 **10x Genomics data and code availability**

534 Jupyter notebooks with custom python scripts for scRNA-seq analysis will be made available in a github  
535 repository upon publication (<https://github.com/theislab/>). 10X Genomics and Smart-seq2 data have  
536 been submitted to GEO and will be made available upon publication.

537

### 538 **Library preparation for Smart-seq2 platform**

539 The 96-well plates containing the sorted pools were first thawed and then incubated for 3 min at 72°C  
540 and thereafter immediately placed on ice. To perform reverse transcription (RT), we added each well a  
541 mix of 0.59 μL H2O, 0.5 μL SMARTScribe™ Reverse Transcriptase (Clontech), 2 μL 5x First Strand buffer,  
542 0.25 μL Recombinant RNase Inhibitor (Clontech), 2 μL Betaine (5 M Sigma), 0.5 μL DTT (100 mM), 0.06  
543 μL MgCl2 (1 M Sigma), 0.1 μL Template-switching oligos (TSO) (100 μM  
544 AAGCAGTGGTATCAACGCAGAGTACrGrG+G). Next, RT reaction mixes were incubated at 42°C for 90  
545 min followed by 70°C for 5 min and 10 cycles of 50°C 2 min, 42°C 2 min; finally ending with 70°C for 5  
546 min for enzyme inactivation. Pre-amplification of cDNA was performed by adding 12.5 μL KAPA HiFi  
547 Hotstart 2x (KAPA Biosystems), 2.138 μL H2O, 0.25 μL ISPCR primers (10 μM, 5'  
548 AAGCAGTGGTATCAACGCAGAGT-3), 0.1125 μL Lambda Exonuclease under the following conditions:  
549 37°C for 30 min, 95°C for 3 min, 20 cycles of (98°C for 20 sec, 67°C for 15 sec, 72°C for 4 min), and a  
550 final extension at 72°C for 5 min. Libraries were then cleaned using AMPure bead (Beckman-Coulter)  
551 cleanup at a 0.7:1 ratio of beads to PCR product. Library was assessed by Bio-analyzer (Agilent 2100),  
552 using the High Sensitivity DNA analysis kit, and also fluorometrically using Qubit's DNA HS assay kits  
553 and a Qubit 4.0 Fluorometer (Invitrogen, LifeTechnologies) to measure the concentrations. Samples  
554 were normalized to 160 pg/μL. Sequencing libraries were constructed by using an in-house produced  
555 Tn5 transposase (Picelli et al., 2014). Libraries were barcoded with the Illumina Nextera XT (FC-131-  
556 1096, Illumina) and pooled, then underwent three rounds of AMPure bead (Beckman-Coulter) cleanup  
557 at a 0.8:1 ratio of beads to library. Libraries were sequenced at 2x100 base pairs paired-end on Illumina  
558 HiSeq4000.

559

### 560 **Processing and analyses of Smart-seq2 data**

561 BCL files were demultiplexed with the bcl2fastq software from Illumina. After quality-control with  
562 FastQC, reads were aligned using rnaSTAR (Dobin et al., 2013) to the GRCm38 (mm10) genome with  
563 ERCC synthetic RNA added. Read counts were collected using the parameter "quantMode GeneCounts"  
564 of rnaSTAR and using the unstranded values. From that point, Seurat R v.3 package was used (Stuart  
565 et al., 2019). Low-quality samples were filtered out from the dataset based on a threshold for the  
566 number of genes detected (min 5000, max 12500 unique genes/pool), percentage of mitochondrial  
567 genes (maximum: 1.5 %), percentage of ERCCs (maximum: 0.5 %) and number of reads (between 100k  
568 to 3M). 291 pools passed the quality-control. Gene counts were log normalized using the

569 NormalizeData function of Seurat with a scale factor of 50,000. Dataset were scaled using the  
570 ScaleData function. The top 1000 most variable genes were considered for the rest of the analyses.  
571 The first 13 principal components were kept from the PCA. Differential expression analysis was  
572 performed using DESeq2 (Love et al., 2014) using the FindAllMarkers function of Seurat. Gene ontology  
573 analyses were performed using Metascape (Zhou et al., 2019) using the genes significantly  
574 differentially expressed at adjusted p-value of 5 %. Sample clustering was performed using the 1000  
575 most variable genes. First, Pearson correlation coefficient was calculated between each sample. Then,  
576 hierarchical clustering was performed (hclust function from stats package) on the Euclidian distance  
577 between samples via the dist function from the stats package and using the ward.D2 method.  
578 Conversely, gene clustering was performed similarly starting from the transposed expression matrix.  
579 Gene ontology was then performed on each gene cluster using Metascape (Zhou et al., 2019). Figures  
580 were generated with ggplot2 package (Wickham, 2016).

### 581 **Statistical analysis**

582 Data are expressed as mean  $\pm$  s.e.m. and were analyzed by unpaired Student's t-test (two-tailed) or one-  
583 or two-way ANOVA and post-hoc tests as indicated in the figure legends. Exclusion criteria are  
584 described in the individual method sections. The data for microglia morphology is shown as median  $\pm$   
585 interquartile range and statistical significance was tested using the Wilcoxon rank sum test with  
586 continuity correction and Bonferroni post-hoc correction for multiple testing in R (version 4.0.3).

587

### 588 **Author contributions**

589 C.B.: conceptualization, formal analysis, investigation, methodology, supervision, visualization, writing  
590 – original draft, funding acquisition. A.S: investigation, methodology (stroke surgery, CM injection, T cell  
591 polarization), validation, supervision; S.H: data curation, formal analysis, investigation (microglia  
592 morphology and analysis); K.P: investigation, methodology (engineered T cells, ELISA), formal analysis;  
593 G.L: investigation, methodology (FISH staining and quantification), formal analysis and A.K:  
594 investigation, methodology (T cell polarization). S.T. and F.T. performed the 10x Genomics analysis.  
595 S.B-G and O.G. ran the Smart-seq2 platform and performed the bioinformatics analysis. A.K. and A.P.  
596 performed the *in vitro* polarization of regulatory T cells. A.L.: funding acquisition, supervision, project  
597 administration, conceptualization, manuscript review, and editing.

598

### 599 **Acknowledgments**

600 The authors thank Kerstin Thuß-Silczak and Dr. Monica Weiler for technical support and Michael Heide  
601 and Oliver Weigert for support at the DKTK Nanostring core facility. Graphical schemes in Figures 1, 4  
602 and Supplementary Figure 3 were created with BioRender.com. The study was supported by the  
603 European Research Council (ERC-StG 802305) and the German Research Foundation (DFG) under  
604 Germany's Excellence Strategy (EXC 2145 SyNergy – ID 390857198), through SFB TRR 274 and under  
605 the DFG projects 405358801 (to A.L.), 418128679 (to C.B.) and PE-2681/1-1 (to A.P.). The authors  
606 declare no competing financial interests.

607 **References**

608  
609  
610 Andres RH, Choi R, Pendharkar AV, Gaeta X, Wang N, Nathan JK, Chua JY, Lee SW, Palmer TD,  
611 Steinberg GK, Guzman R. 2011. The CCR2/CCL2 Interaction Mediates the Transendothelial  
612 Recruitment of Intravascularly Delivered Neural Stem Cells to the Ischemic Brain. *Stroke* 42:2923–  
613 2931. doi:10.1161/strokeaha.110.606368

614 Anrather J, Iadecola C. 2016. Inflammation and Stroke: An Overview. *Neurotherapeutics* 13:661–670.  
615 doi:10.1007/s13311-016-0483-x

616 Becht E, McInnes L, Healy J, Dutertre C-A, Kwok IWH, Ng LG, Ginhoux F, Newell EW. 2019.  
617 Dimensionality reduction for visualizing single-cell data using UMAP. *Nat Biotechnol* 37:38–44.  
618 doi:10.1038/nbt.4314

619 Benakis C, Brea D, Caballero S, Faraco G, Moore J, Murphy M, Sita G, Racchumi G, Ling L, Pamer EG,  
620 Iadecola C, Anrather J. 2016. Commensal microbiota affects ischemic stroke outcome by  
621 regulating intestinal  $\gamma\delta$  T cells. *Nat Med* 22:516–523. doi:10.1038/nm.4068

622 Benakis C, Llovera G, Liesz A. 2018. The meningeal and choroidal infiltration routes for leukocytes in  
623 stroke. *Ther Adv Neurol Diso* 11:1756286418783708. doi:10.1177/1756286418783708

624 Bindea G, Mlecnik B, Hackl H, Charoentong P, Tosolini M, Kirilovsky A, Fridman W-H, Pagès F,  
625 Trajanoski Z, Galon J. 2009. ClueGO: a Cytoscape plug-in to decipher functionally grouped gene  
626 ontology and pathway annotation networks. *Bioinformatics* 25:1091–1093.  
627 doi:10.1093/bioinformatics/btp101

628 Blondel VD, Guillaume J-L, Lambiotte R, Lefebvre E. 2008. Fast unfolding of communities in large  
629 networks. *J Statistical Mech Theory Exp* 2008:P10008. doi:10.1088/1742-5468/2008/10/p10008

630 Chabot S, Williams G, Hamilton M, Sutherland G, Yong VW. 1999. Mechanisms of IL-10 production in  
631 human microglia-T cell interaction. *J Immunol Baltim Md* 1950 162:6819–28.

632 Cramer JV, Benakis C, Liesz A. 2018. T cells in the post-ischemic brain: Troopers or paramedics? *J  
633 Neuroimmunol* 326:33–37. doi:10.1016/j.jneuroim.2018.11.006

634 Cserép C, Pósfai B, Lénárt N, Fekete R, László ZI, Lele Z, Orsolits B, Molnár G, Heindl S, Schwarcz AD,  
635 Ujvári K, Környei Z, Tóth K, Szabadits E, Sperlágh B, Baranyi M, Csiba L, Hortobágyi T, Maglóczky Z,  
636 Martinecz B, Szabó G, Erdélyi F, Szipőcs R, Tamkun MM, Gesierich B, Duering M, Katona I, Liesz A,  
637 Tamás G, Dénes Á. 2020. Microglia monitor and protect neuronal function through specialized  
638 somatic purinergic junctions. *Science* 367:528–537. doi:10.1126/science.aax6752

639 Dirnagl U, Iadecola C, Moskowitz MA, Dirnagl U, Iadecola C, Moskowitz MA. 1999. Pathobiology of  
640 ischaemic stroke: an integrated view. *Trends Neurosci* 22:391–397. doi:10.1016/s0166-  
641 2236(99)01401-0

642 Dobin A, Davis CA, Schlesinger F, Drenkow J, Zaleski C, Jha S, Batut P, Chaisson M, Gingeras TR.  
643 2013. STAR: ultrafast universal RNA-seq aligner. *Bioinformatics* 29:15–21.  
644 doi:10.1093/bioinformatics/bts635

645 Dong Y, Yong VW. 2019. When encephalitogenic T cells collaborate with microglia in multiple  
646 sclerosis. *Nat Rev Neurol* 15:704–717. doi:10.1038/s41582-019-0253-6

647 Filiano AJ, Gadani SP, Kipnis J. 2017. How and why do T cells and their derived cytokines affect the  
648 injured and healthy brain? *Nat Rev Neurosci* 18:375–384. doi:10.1038/nrn.2017.39

649 Garcia-Bonilla L, Benakis C, Moore J, Iadecola C, Anrather J. 2014. Immune mechanisms in cerebral  
650 ischemic tolerance. *Front Neurosci-switz* 8:44. doi:10.3389/fnins.2014.00044

651 Gelderblom M, Leypoldt F, Steinbach K, Behrens D, Choe C-U, Siler DA, Arumugam TV, Orthay E, Gerloff  
652 C, Tolosa E, Magnus T. 2009. Temporal and Spatial Dynamics of Cerebral Immune Cell  
653 Accumulation in Stroke. *Stroke* 40:1849–1857. doi:10.1161/strokeaha.108.534503

654 Gelderblom M, Weymar A, Bernreuther C, Velden J, Arunachalam P, Steinbach K, Orthay E, Arumugam  
655 TV, Leypoldt F, Simova O, Thom V, Friese MA, Prinz I, Hölscher C, Glatzel M, Korn T, Gerloff C,  
656 Tolosa E, Magnus T. 2012. Neutralization of the IL-17 axis diminishes neutrophil invasion and  
657 protects from ischemic stroke. *Blood* 120:3793–3802. doi:10.1182/blood-2012-02-412726

658 Goldmann T, Prinz M. 2013. Role of Microglia in CNS Autoimmunity. *Clin Dev Immunol* 2013:1–8.  
659 doi:10.1155/2013/208093

660 Haghverdi L, Büttner M, Wolf FA, Buettner F, Theis FJ. 2016. Diffusion pseudotime robustly  
661 reconstructs lineage branching. *Nat Methods* 13:845–848. doi:10.1038/nmeth.3971

662 Heindl S, Gesierich B, Benakis C, Llovera G, Duering M, Liesz A. 2018. Automated Morphological  
663 Analysis of Microglia After Stroke. *Front Cell Neurosci* 12:106. doi:10.3389/fncel.2018.00106

664 Heindl S, Ricci A, Carofiglio O, Zhou Q, Arzberger T, Lenart N, Franzmeier N, Hortobagyi T, Nelson PT,  
665 Stowe AM, Denes A, Edbauer D, Liesz A. 2021. Chronic T cell proliferation in brains after stroke  
666 could interfere with the efficacy of immunotherapies. *J Exp Med* 218:e20202411.  
667 doi:10.1084/jem.20202411

668 Iliff JJ, Wang M, Liao Y, Plogg BA, Peng W, Gundersen GA, Benveniste H, Vates GE, Deane R, Goldman  
669 SA, Nagelhus EA, Nedergaard M. 2012. A Paravascular Pathway Facilitates CSF Flow Through the  
670 Brain Parenchyma and the Clearance of Interstitial Solutes, Including Amyloid  $\beta$ . *Sci Transl Med*  
671 4:147ra111-147ra111. doi:10.1126/scitranslmed.3003748

672 Keren-Shaul H, Spinrad A, Weiner A, Matcovitch-Natan O, Dvir-Szternfeld R, Ulland TK, David E, Baruch  
673 K, Lara-Astaiso D, Toth B, Itzkovitz S, Colonna M, Schwartz M, Amit I. 2017. A Unique Microglia  
674 Type Associated with Restricting Development of Alzheimer's Disease. *Cell* 169:1276–1290.e17.  
675 doi:10.1016/j.cell.2017.05.018

676 Kilkenny C, Browne W, Cuthill IC, Emerson M, Altman DG, Research NC for the R Refinement and  
677 Reduction of Animals in. 2011. Animal Research: Reporting in vivo Experiments—The ARRIVE  
678 Guidelines. *J Cereb Blood Flow Metabolism* 31:991–993. doi:10.1038/jcbfm.2010.220

679 Kleinschmitz C, Schwab N, Kraft P, Hagedorn I, Dreykluft A, Schwarz T, Austinat M, Nieswandt B,  
680 Wiendl H, Stoll G. 2010. Early detrimental T-cell effects in experimental cerebral ischemia are  
681 neither related to adaptive immunity nor thrombus formation. *Blood* 115:3835–3842.  
682 doi:10.1182/blood-2009-10-249078

683 Le T, Leung L, Carroll WL, Schibler KR. 1997. Regulation of interleukin-10 gene expression: possible  
684 mechanisms accounting for its upregulation and for maturational differences in its expression by  
685 blood mononuclear cells. *Blood* 89:4112–9.

686 Lee Y, Awasthi A, Yosef N, Quintana FJ, Xiao S, Peters A, Wu C, Kleinewietfeld M, Kunder S, Hafler DA,  
687 Sobel RA, Regev A, Kuchroo VK. 2012. Induction and molecular signature of pathogenic TH17  
688 cells. *Nat Immunol* 13:991–999. doi:10.1038/ni.2416

689 Liesz A, Bauer A, Hoheisel JD, Veltkamp R. 2014. Intracerebral interleukin-10 injection modulates  
690 post-ischemic neuroinflammation: An experimental microarray study. *Neurosci Lett* 579:18–23.  
691 doi:10.1016/j.neulet.2014.07.003

692 Liesz A, Suri-Payer E, Veltkamp C, Doerr H, Sommer C, Rivest S, Giese T, Veltkamp R. 2009. Regulatory  
693 T cells are key cerebroprotective immunomodulators in acute experimental stroke. *Nat Med*  
694 15:192–199. doi:10.1038/nm.1927

695 Liesz A, Zhou W, Mracskó É, Karcher S, Bauer H, Schwarting S, Sun L, Bruder D, Stegemann S,  
696 Cerwenka A, Sommer C, Dalpke AH, Veltkamp R. 2011. Inhibition of lymphocyte trafficking shields  
697 the brain against deleterious neuroinflammation after stroke. *Brain* 134:704–720.  
698 doi:10.1093/brain/awr008

699 Liu XS, Zhang ZG, Zhang RL, Gregg SR, Wang L, Yier T, Chopp M. 2007. Chemokine ligand 2 (CCL2)  
700 induces migration and differentiation of subventricular zone cells after stroke. *J Neurosci Res*  
701 85:2120–2125. doi:10.1002/jnr.21359

702 Llovera G, Benakis C, Enzmann G, Cai R, Arzberger T, Ghasemigharagoz A, Mao X, Malik R, Lazarevic I,  
703 Liebscher S, Ertürk A, Meissner L, Vivien D, Haffner C, Plesnila N, Montaner J, Engelhardt B, Liesz  
704 A. 2017. The choroid plexus is a key cerebral invasion route for T cells after stroke. *Acta  
705 Neuropathol* 134:851–868. doi:10.1007/s00401-017-1758-y

706 Llovera G, Hofmann K, Roth S, Salas-Pérdomo A, Ferrer-Ferrer M, Perego C, Zanier ER, Mamrak U, Rex  
707 A, Party H, Agin V, Fauchon C, Orset C, Haelewyn B, Simoni M-GD, Dirnagl U, Grittner U, Planas AM,  
708 Plesnila N, Vivien D, Liesz A. 2015. Results of a preclinical randomized controlled multicenter trial  
709 (pRCT): Anti-CD49d treatment for acute brain ischemia. *Sci Transl Med* 7:299ra121-299ra121.  
710 doi:10.1126/scitranslmed.aaa9853

711 Llovera G, Roth S, Plesnila N, Veltkamp R, Liesz A. 2014. Modeling Stroke in Mice: Permanent  
712 Coagulation of the Distal Middle Cerebral Artery. *J Vis Exp Jove* 51729. doi:10.3791/51729

713 Love MI, Huber W, Anders S. 2014. Moderated estimation of fold change and dispersion for RNA-seq  
714 data with DESeq2. *Genome Biol* 15:550. doi:10.1186/s13059-014-0550-8

715 Luecken MD, Theis FJ. 2019. Current best practices in single-cell RNA-seq analysis: a tutorial. *Mol  
716 Syst Biol* 15:e8746. doi:10.15252/msb.20188746

717 Mathys H, Adaikkan C, Gao F, Young JZ, Manet E, Hemberg M, Jager PLD, Ransohoff RM, Regev A,  
718 Tsai L-H. 2017. Temporal Tracking of Microglia Activation in Neurodegeneration at Single-Cell  
719 Resolution. *Cell Reports* 21:366–380. doi:10.1016/j.celrep.2017.09.039

720 Miron VE, Priller J. 2020. Investigating Microglia in Health and Disease: Challenges and Opportunities.  
721 *Trends Immunol* 41:785–793. doi:10.1016/j.it.2020.07.002

722 Picelli S, Faridani OR, Björklund ÅK, Winberg G, Sagasser S, Sandberg R. 2014. Full-length RNA-seq  
723 from single cells using Smart-seq2. *Nat Protoc* 9:171–181. doi:10.1038/nprot.2014.006

724 Prinz M, Priller J. 2014. Microglia and brain macrophages in the molecular age: from origin to  
725 neuropsychiatric disease. *Nat Rev Neurosci* 15:300–312. doi:10.1038/nrn3722

726 Roth S, Yang J, Cramer J, Malik R, Liesz A. 2020. Detection of cytokine-induced sickness behavior  
727 after ischemic stroke by an optimized behavioral assessment battery. *Brain Behav Immun* 91:668–  
728 672. doi:10.1016/j.bbi.2020.11.016

729 Saraiva M, Vieira P, O'Garra A. 2019. Biology and therapeutic potential of interleukin-10. *J Exp Med*  
730 217:e20190418. doi:10.1084/jem.20190418

731 Satija R, Farrell JA, Gennert D, Schier AF, Regev A. 2015. Spatial reconstruction of single-cell gene  
732 expression data. *Nat Biotechnol* 33:495–502. doi:10.1038/nbt.3192

733 Saxena A, Khosraviani S, Noel S, Mohan D, Donner T, Hamad ARA. 2015. Interleukin-10 paradox: A  
734 potent immunoregulatory cytokine that has been difficult to harness for immunotherapy. *Cytokine*  
735 74:27–34. doi:10.1016/j.cyto.2014.10.031

736 Schafer DP, Lehrman EK, Kautzman AG, Koyama R, Mardinly AR, Yamasaki R, Ransohoff RM,  
737 Greenberg ME, Barres BA, Stevens B. 2012. Microglia Sculpt Postnatal Neural Circuits in an  
738 Activity and Complement-Dependent Manner. *Neuron* 74:691–705.  
739 doi:10.1016/j.neuron.2012.03.026

740 Shemer A, Scheyltjens I, Frumer GR, Kim J-S, Grozovski J, Ayanaw S, Dassa B, Hove HV, Chappell-  
741 Maor L, Boura-Halfon S, Leshkowitz D, Mueller W, Maggio N, Movahedi K, Jung S. 2020.  
742 Interleukin-10 Prevents Pathological Microglia Hyperactivation following Peripheral Endotoxin  
743 Challenge. *Immunity* 53:1033–1049.e7. doi:10.1016/j.immuni.2020.09.018

744 Shi L, Sun Z, Su W, Xu F, Xie D, Zhang Q, Dai X, Iyer K, Hitchens TK, Foley LM, Li S, Stoltz DB, Chen K,  
745 Ding Y, Thomson AW, Leak RK, Chen J, Hu X. 2021. Treg cell-derived osteopontin promotes  
746 microglia-mediated white matter repair after ischemic stroke. *Immunity* 54:1527–1542.e8.  
747 doi:10.1016/j.immuni.2021.04.022

748 Shichita T, Sugiyama Y, Ooboshi H, Sugimori H, Nakagawa R, Takada I, Iwaki T, Okada Y, Iida M, Cua  
749 DJ, Iwakura Y, Yoshimura A. 2009. Pivotal role of cerebral interleukin-17-producing  $\gamma\delta T$  cells in  
750 the delayed phase of ischemic brain injury. *Nat Med* 15:946–950. doi:10.1038/nm.1999

751 Stephan AH, Barres BA, Stevens B. 2012. The Complement System: An Unexpected Role in Synaptic  
752 Pruning During Development and Disease. *Neuroscience* 35:369–389. doi:10.1146/annurev-neuro-  
753 061010-113810

754 Stuart T, Butler A, Hoffman P, Hafemeister C, Papalex E, Mauck WM, Hao Y, Stoeckius M, Smibert P,  
755 Satija R. 2019. Comprehensive Integration of Single-Cell Data. *Cell* 177:1888–1902.e21.  
756 doi:10.1016/j.cell.2019.05.031

757 Szalay G, Martinecz B, Lénárt N, Környei Z, Orsolits B, Judák L, Császár E, Fekete R, West BL, Katona G,  
758 Rózsa B, Dénes Á. 2016. Microglia protect against brain injury and their selective elimination  
759 dysregulates neuronal network activity after stroke. *Nat Commun* 7:11499.  
760 doi:10.1038/ncomms11499

761 Virtanen P, Gommers R, Oliphant TE, Haberland M, Reddy T, Cournapeau D, Burovski E, Peterson P,  
762 Weckesser W, Bright J, Walt SJ van der, Brett M, Wilson J, Millman KJ, Mayorov N, Nelson ARJ,  
763 Jones E, Kern R, Larson E, Carey CJ, Polat İ, Feng Y, Moore EW, VanderPlas J, Laxalde D, Perktold  
764 J, Cimrman R, Henriksen I, Quintero EA, Harris CR, Archibald AM, Ribeiro AH, Pedregosa F,  
765 Mulbregt P van, Vijaykumar A, Bardelli AP, Rothberg A, Hilboll A, Kloeckner A, Scopatz A, Lee A,  
766 Rokem A, Woods CN, Fulton C, Masson C, Häggström C, Fitzgerald C, Nicholson DA, Hagen DR,  
767 Pasechnik DV, Olivetti E, Martin E, Wieser E, Silva F, Lenders F, Wilhelm F, Young G, Price GA, Ingold  
768 G-L, Allen GE, Lee GR, Audren H, Probst I, Dietrich JP, Silterra J, Webber JT, Slavič J, Nothman J,  
769 Buchner J, Kulick J, Schönberger JL, Cardoso JV de M, Reimer J, Harrington J, Rodríguez JLC,  
770 Nunez-Iglesias J, Kuczynski J, Tritz K, Thoma M, Newville M, Kümmeler M, Bolingbroke M, Tartre  
771 M, Pak M, Smith NJ, Nowaczyk N, Shebanov N, Pavlyk O, Brodtkorb PA, Lee P, McGibbon RT,  
772 Feldbauer R, Lewis S, Tygier S, Sievert S, Vigna S, Peterson S, More S, Pudlik T, Oshima T, Pingel  
773 TJ, Robitaille TP, Spura T, Jones TR, Cera T, Leslie T, Zito T, Krauss T, Upadhyay U, Halchenko YO,  
774 Vázquez-Baeza Y. 2020. Author Correction: SciPy 1.0: fundamental algorithms for scientific  
775 computing in Python. *Nat Methods* 17:352–352. doi:10.1038/s41592-020-0772-5

776 Wang S, Zhang H, Xu Y. 2016. Crosstalk between microglia and T cells contributes to brain damage  
777 and recovery after ischemic stroke. *Neurol Res* 38:495–503. doi:10.1080/01616412.2016.1188473

778 Wickham H. 2016. ggplot2, Elegant Graphics for Data Analysis. *R* 147–168. doi:10.1007/978-3-319-  
779 24277-4\_7

780 Wolf FA, Angerer P, Theis FJ. 2018. SCANPY: large-scale single-cell gene expression data analysis.  
781 *Genome Biol* 19:15. doi:10.1186/s13059-017-1382-0

782 Wolock SL, Lopez R, Klein AM. 2019. Scrublet: Computational Identification of Cell Doublets in Single-  
783 Cell Transcriptomic Data. *Cell Syst* 8:281-291.e9. doi:10.1016/j.cels.2018.11.005

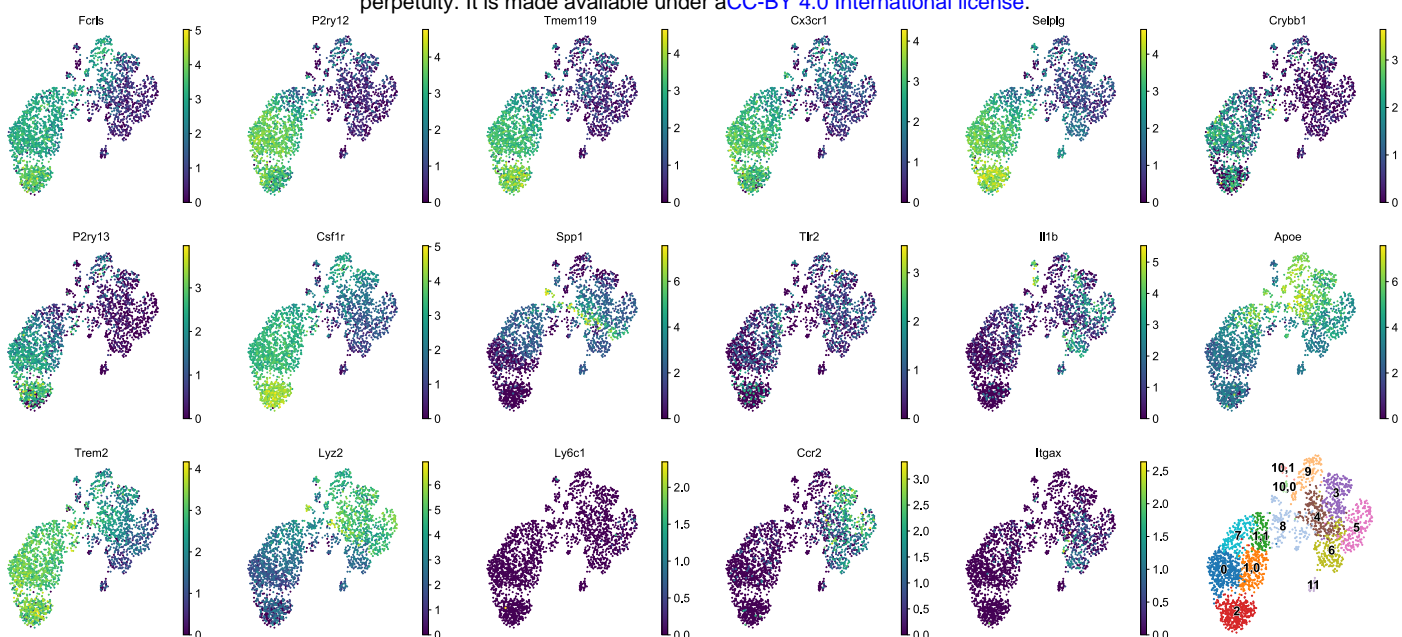
784 Xie Z, Bailey A, Kuleshov MV, Clarke DJB, Evangelista JE, Jenkins SL, Lachmann A, Wojciechowicz ML,  
785 Kropiwnicki E, Jagodnik KM, Jeon M, Ma'ayan A. 2021. Gene Set Knowledge Discovery with  
786 Enrichr. *Curr Protoc* 1:e90. doi:10.1002/cpz1.90

787 Zaki Y, Cai DJ. 2020. Creating Space for Synaptic Formation—A New Role for Microglia in Synaptic  
788 Plasticity. *Cell* 182:265–267. doi:10.1016/j.cell.2020.06.042

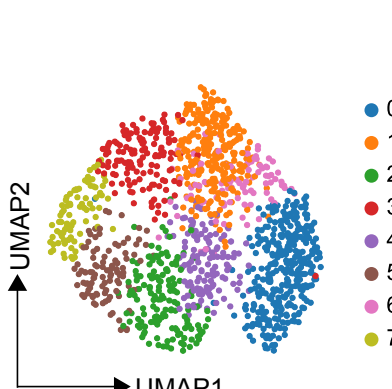
789 Zhou Y, Zhou B, Pache L, Chang M, Khodabakhshi AH, Tanaseichuk O, Benner C, Chanda SK. 2019.  
790 Metascape provides a biologist-oriented resource for the analysis of systems-level datasets. *Nat  
791 Commun* 10:1523. doi:10.1038/s41467-019-09234-6

792

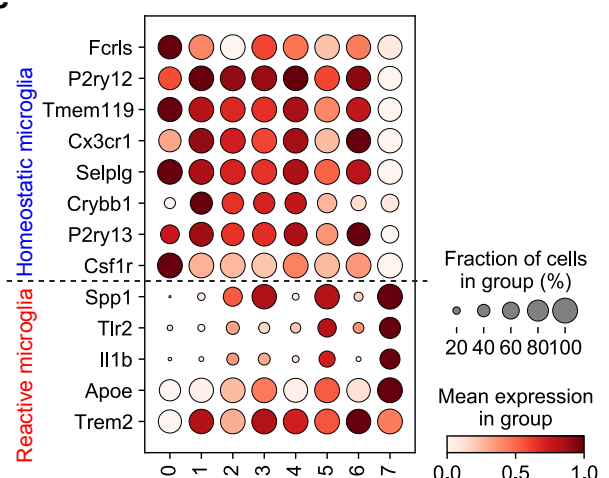
a



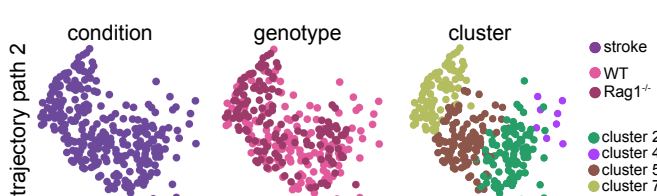
b



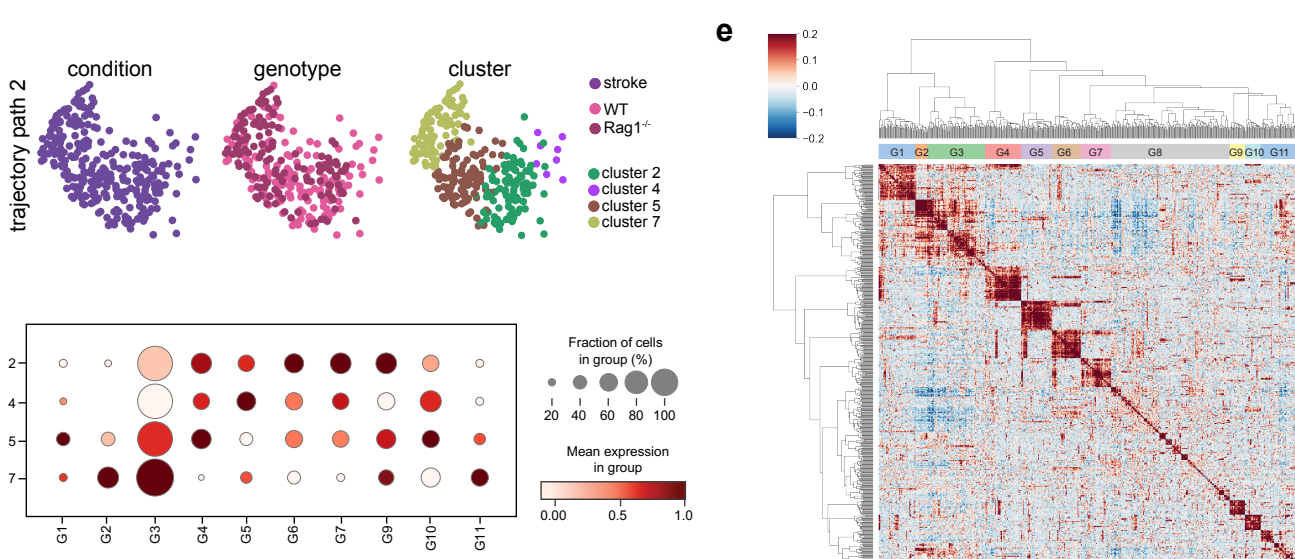
c



d

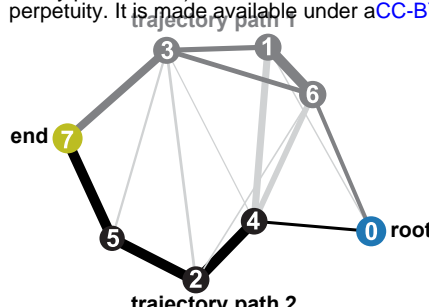
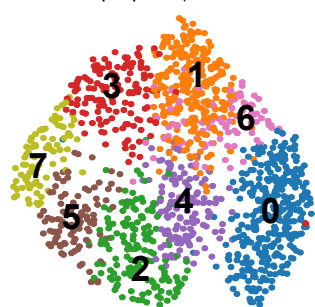


e

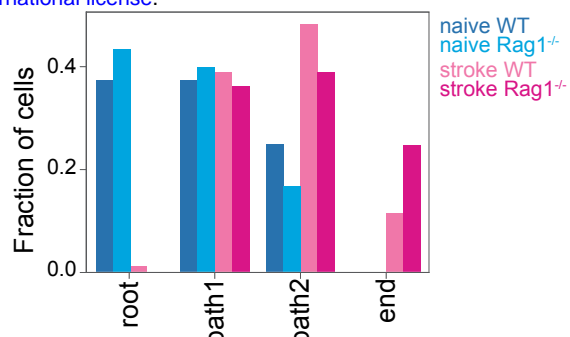


**Supplementary Fig. 1 Transcriptomic analysis of microglia isolated from WT and Rag1<sup>-/-</sup> in naïve and stroke conditions.** **a** UMAP plots showing expression of known CD45+CD11b+ myeloid cell marker genes and Louvain-clusters. **b,c** Manifold and clustering of microglia: **b** UMAP plots indicate Louvain-clusters of microglial cells. **c** Dot plots show gene expression distribution of marker genes split by Louvain-cluster, and their grouping into homeostatic (top) and reactive (bottom) microglia. **d–e** Microglia gene set expression in stroke condition. **d** UMAP plots in path 2 and end cell clusters colored-coded by stroke condition (left), genotype (middle) and clusters (right). **e** Gene-gene correlation map of the correlated and anti-correlated genes extracted from clusters 2, 4, 5 and 7 identified 11 gene clusters. Due to low correlation, G8 was excluded of further analysis. **f** Dot plots show gene set expression distribution (G1 to G11) of the stroke cell clusters (2, 4, 5, 7).

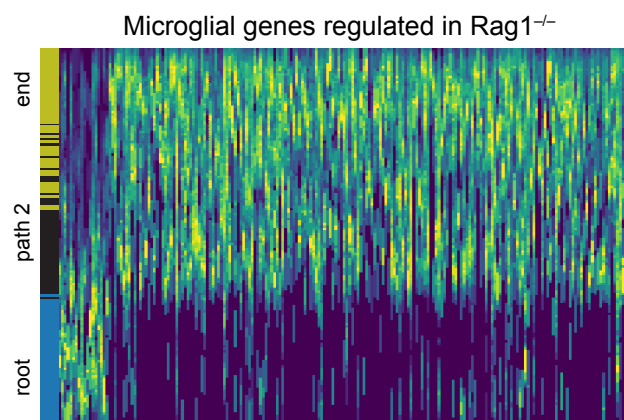
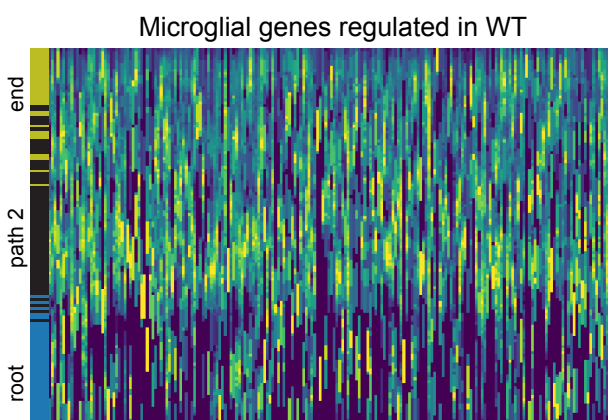
a



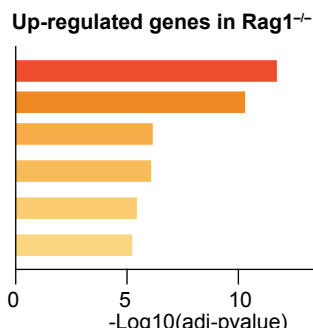
b



c



d

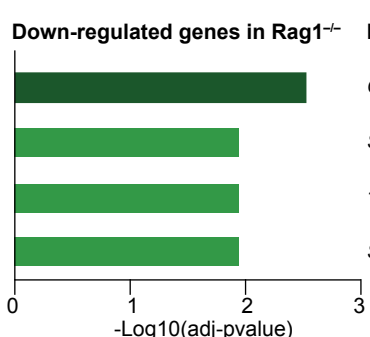


Marker genes

*Mrpl50, Mrpl40, Mrpl49, Mrpl9, Mrpl12, Mrpl46, Mrrf, Mrpl21, Mrpl44*  
*Mrpl50, Mrpl40, Mrpl49, Mrpl9, Mrpl12, Mrpl46, Mrpl21, Mrpl44*  
*Ltv1, Exosc5, Exosc9, Pih1d1, Fcf1, Utp18, Rpf1*  
*Exosc5, Exosc9, Pih1d1, Fcf1, Utp18, Mrp44, Rpf1*  
*Upf1, Usp7, Dhx36, Pml*  
*Exosc5, Exosc9, Pih1d1, Fcf1, Utp18, Rpf1*

Top enriched pathways

mitochondrial translational termination  
mitochondrial translational elongation  
ribosome biogenesis  
ncRNA processing  
regulation of telomere maintenance  
rRNA metabolic process



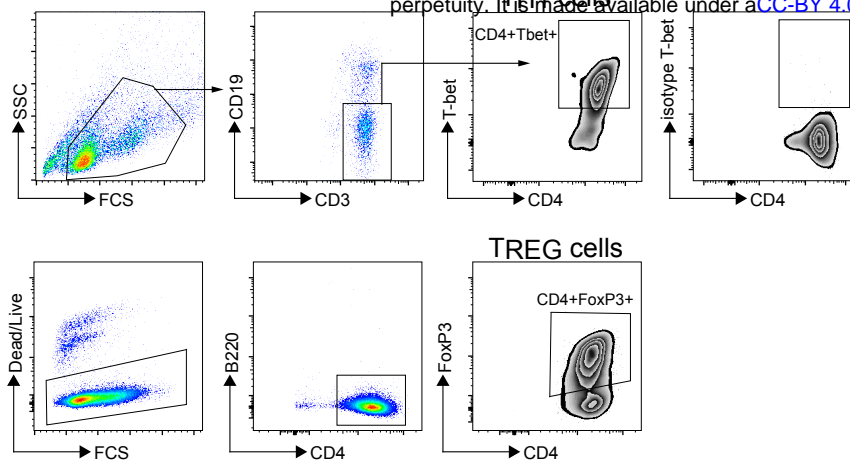
Marker genes

Top enriched pathways

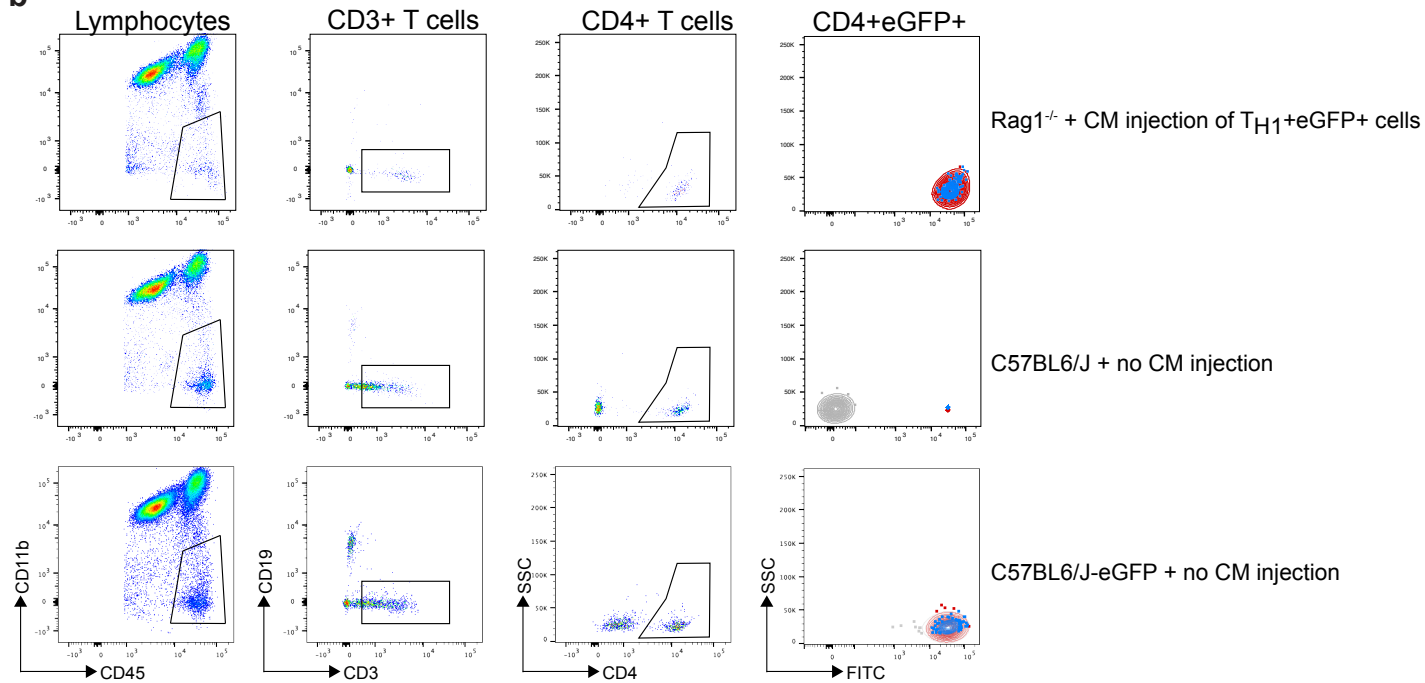
*C1stn1, Tgm2* phagocytosis, positive regulation of nervous system development  
*S100a9* chronic inflammatory response, regulation of integrin biosynthetic process, astrocyte development, peptidyl-cysteine S-nitrosylation  
*Tgm2* negative regulation of endoplasmic reticulum calcium ion concentration, response to cocaine  
*Stard5* sterol import, cholesterol import

**Supplementary Fig. 2 Microglia single cell trajectory inference in WT and  $Rag1^{-/-}$  naïve and stroke conditions.** **a,b** Microglia single cell trajectory inference describes the evolution of microglia activation from naïve to stroke condition. **a** Partition-based graph abstraction graph (PAGA, right) shows cluster connectivity of Louvain-clusters (left) with a threshold of 0.1. Nodes represent subsets, and thicker edges indicate stronger connectedness between subsets. The trajectories path 1 and 2 are selected based on the connectivity (edge width) in the PAGA graph after the root and end paths were defined based on marker gene expression. Clusters along the paths from root-to-end were merged since these are consecutive. Trajectory path 1 (dark grey): root (cluster 0), path 1 (cluster 6, 1, 3 merged), end (cluster 7); trajectory path 2 (black): root (cluster 0), path 2 (cluster 4, 2, 5 merged), end (cluster 7). **b** Barplot shows cell frequencies split by condition in trajectories path 1 and path 2. **c,d** Differential microglial gene expression analysis between root and end clusters along trajectory path 2. **c** Heatmaps show scaled expression along path 2 trajectory of microglial genes specifically regulated in  $Rag1^{-/-}$  and compared in WT (left) and  $Rag1^{-/-}$  (right) in path 2 (Wilcoxon test, adjusted  $P < 0.05$ ). For balanced representation of cells along the trajectory root and path 2, cells were randomly subset to 100 cells before plotting. **d** Top enriched pathways of microglial genes up- and down-regulated in  $Rag1^{-/-}$  mice.

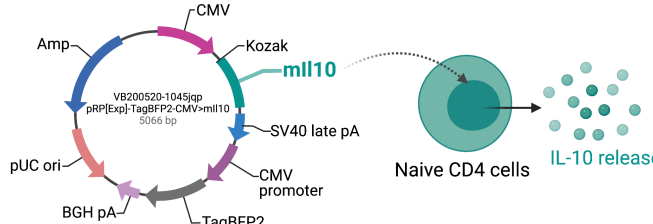
a



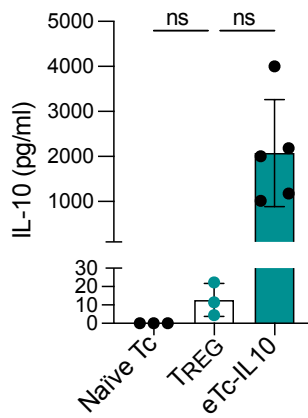
b



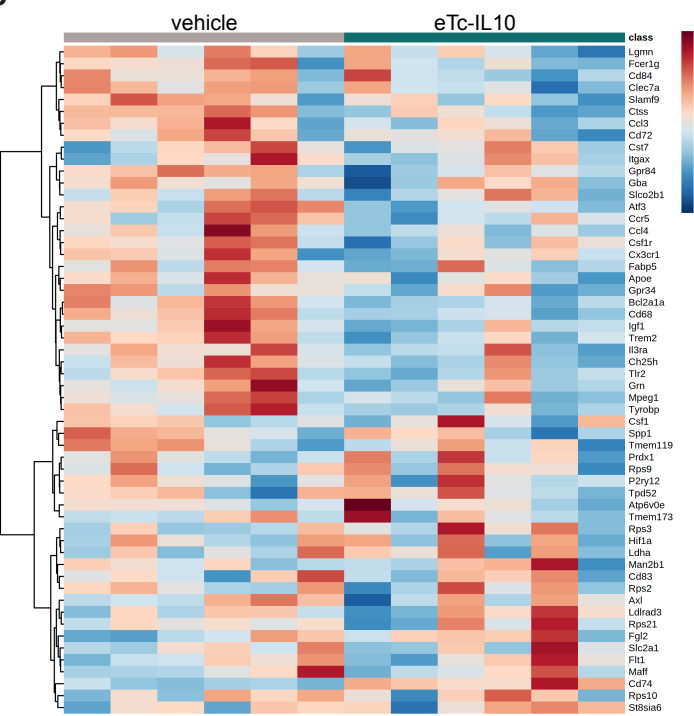
c



d



e



**Supplementary Fig. 3 T cell polarization *in vitro* and IL-10 plasmid construct.** **a** CD4 naïve T cells were polarized *in vitro* towards TH1 (top row, CD4+Tbet+) or TREG (bottom row, CD4 +FoxP3+). **b** Gating strategy of CD4<sup>+</sup>eGFP<sup>+</sup> cells analyzed by flow cytometry in the ipsilateral (red) and contralateral (blue) hemispheres (CD45<sup>+</sup>CD11b<sup>-</sup>CD19<sup>-</sup>CD3<sup>+</sup>CD4<sup>+</sup>FITC<sup>+</sup>) in Rag1<sup>-/-</sup> (top row), C57BL6/J (no cell injection, mid-row) and in C57BL6/J actin-eGFP mice (no cell injection, bottom row). **c** Plasmid expression vector pIL-10 was constructed by inserting 537bp IL-10 cDNA under a CMV promoter with a BFP2 tag and ampicillin resistance. **d** IL-10 concentration measured by ELISA in naïve T cells, TREG cells and naïve T cell transfected with pIL-10 (eTc-IL10); ns, non significant; \*, P < 0.05. **e** Heatmap representation of brain gene expression between vehicle and eTc-IL10 treated mice selected from the known disease-associated microglial genes (Keren-Shaul et al., 2017).

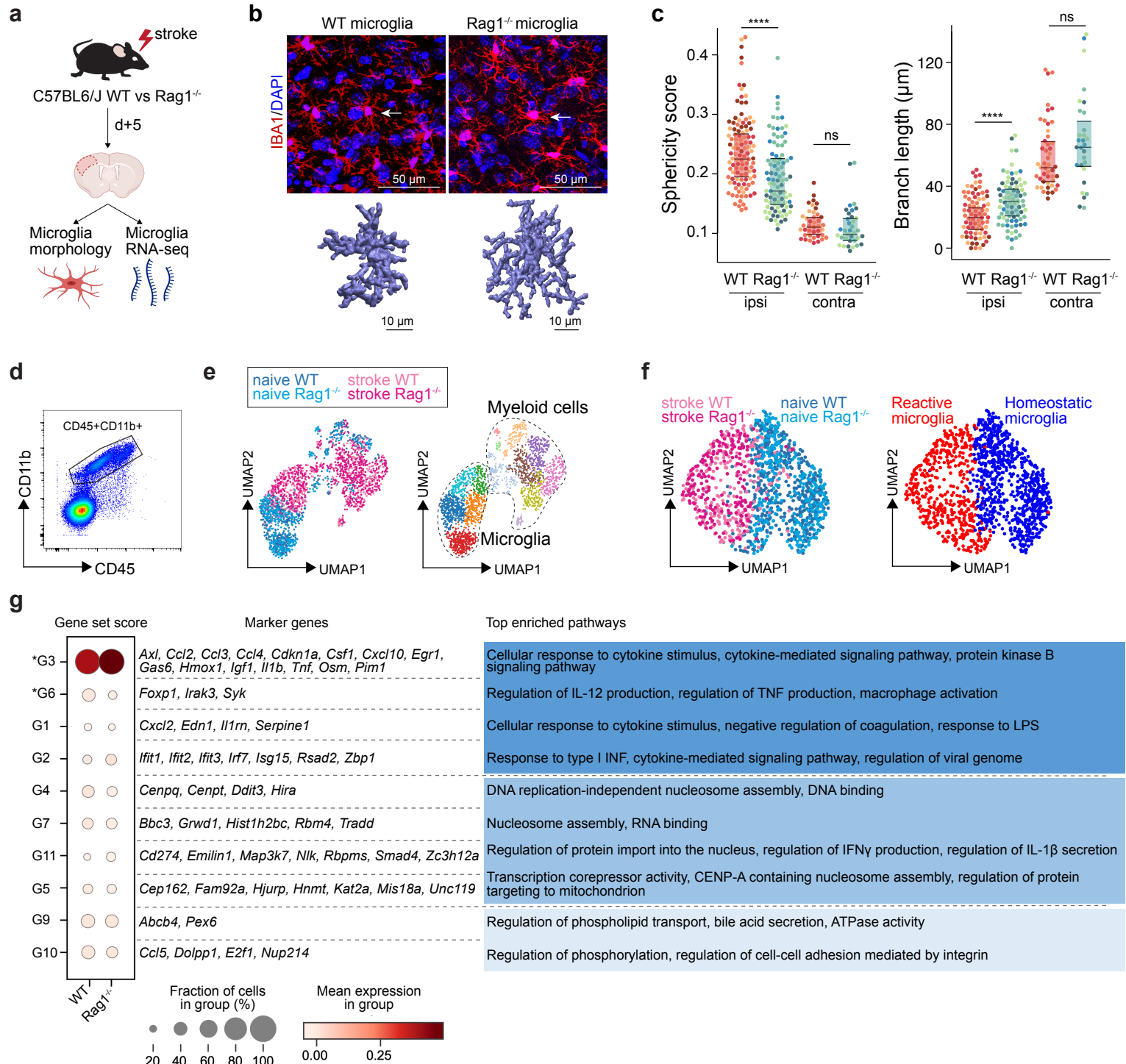
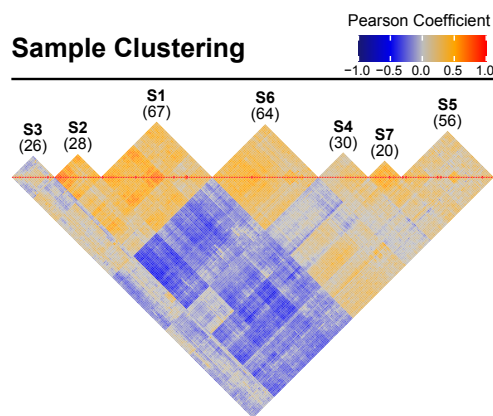


**Figure 1. T cells influence microglia morphology and transcriptomic signature.** **a** Morphological analysis of microglia and transcriptomic profile of sorted microglia were performed 5 d after stroke in wild-type (WT) and Rag1<sup>-/-</sup> mice. **b** Top, representative images of IBA1+ microglial cells in the perilesional region (900 μm distal to the infarct border, cortical layer 4). Bottom, three-dimensional (3D) reconstruction of microglia in WT and Rag1<sup>-/-</sup> mice. **c** Morphological analysis of microglia in the peri-infarct area (ipsi) and in the contralateral hemisphere (contra) for two representative features: sphericity and branch length (μm) in WT (orange) and Rag1<sup>-/-</sup> (blue) mice. Each individual mouse is represented in the plots by one color (4 mice/condition), each dot corresponds to one microglial cell; ns, non significant; \*\*\*, P < 0.0001. Wilcoxon rank sum test with continuity correction and Bonferroni post-hoc correction for multiple testing. **d** CD45+CD11b+ cells were sorted from the ipsilateral hemisphere 5 d after stroke in WT and Rag1<sup>-/-</sup> (3 mice/condition) and RNA was isolated for single cell RNA sequencing (10x Genomics). **e** Uniform manifold approximation and projection 2D space (UMAP) plots of 2345 CD45+CD11b+ cells colored by conditions (left) and by 14 distinct transcriptional clusters (right and Supplementary Fig. 1). **f** Clustering of the microglia subset color-coded by conditions (left) and into homeostatic and reactive microglia (right). **g** Selected gene sets of highly correlated and anti-correlated genes based on trajectory inference analysis in stroke condition (Supplementary Fig. 1d-f). Mean gene set activation score in WT and Rag1<sup>-/-</sup> cells, selected marker genes and top enriched gene ontology pathways associated to each gene set. Gene sets were classified by p-value (the lowest p-value at the top, asterisks (\*) indicate significant difference between genotype in stroke condition) and by similar pathways, such as: pathways related to inflammation (dark blue), pathways related to DNA/RNA regulation (blue) and lipid pathways (light blue).

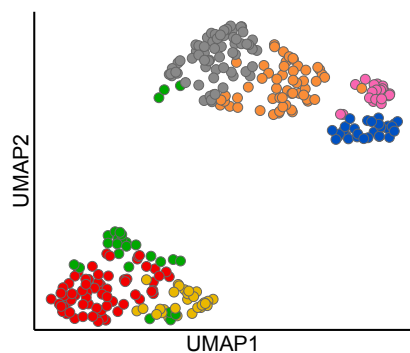
a



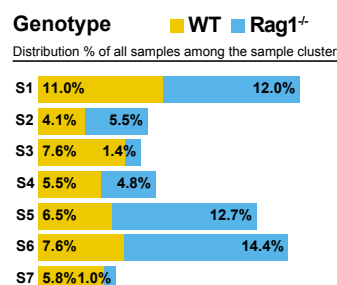
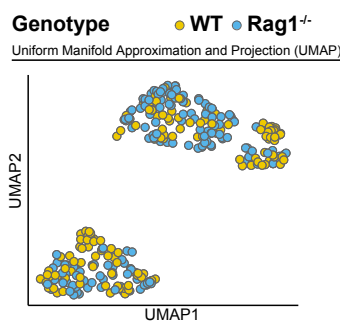
### Hierarchical Clustering

UMAP coloured by identified sample cluster (Ward's method)

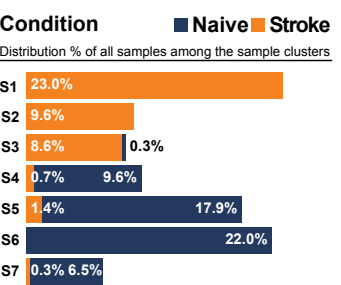
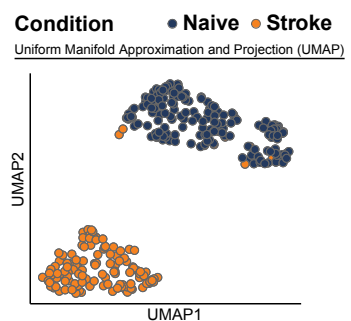
● S1 ● S2 ● S3 ● S4 ● S5 ● S6 ● S7



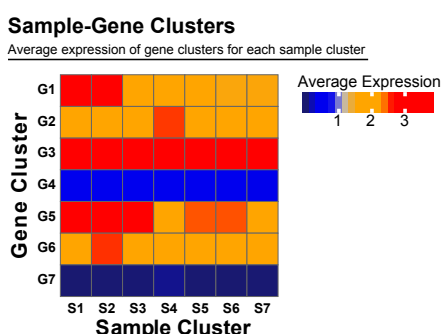
c



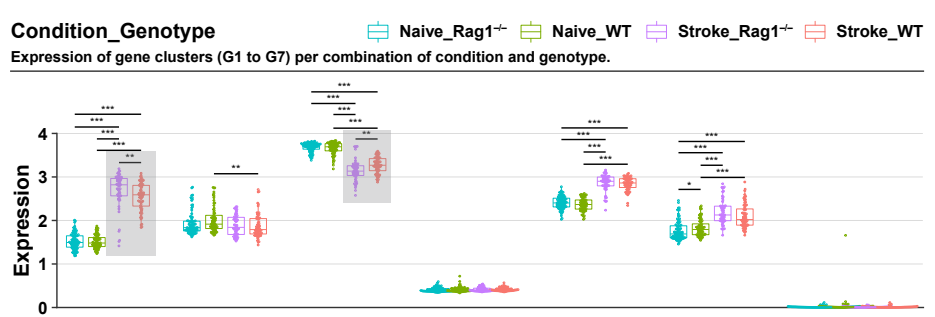
d



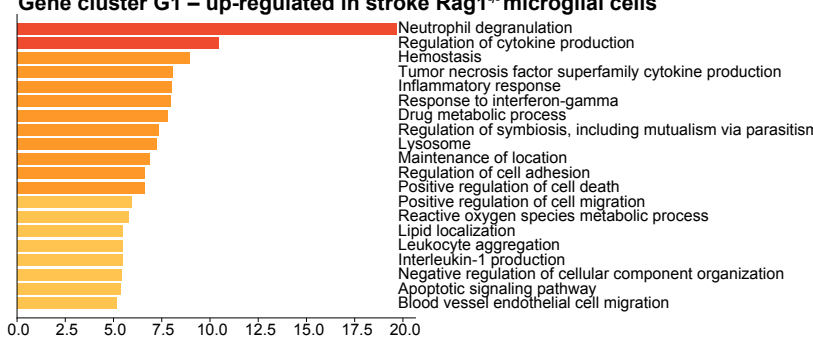
e



f



g Gene cluster G1 – up-regulated in stroke *Rag1*<sup>-/-</sup> microglial cells



Gene Cluster G3 – down-regulated in stroke *Rag1*<sup>-/-</sup> microglial cells

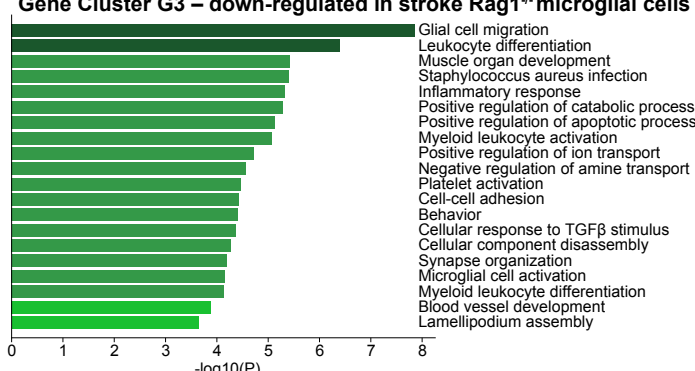
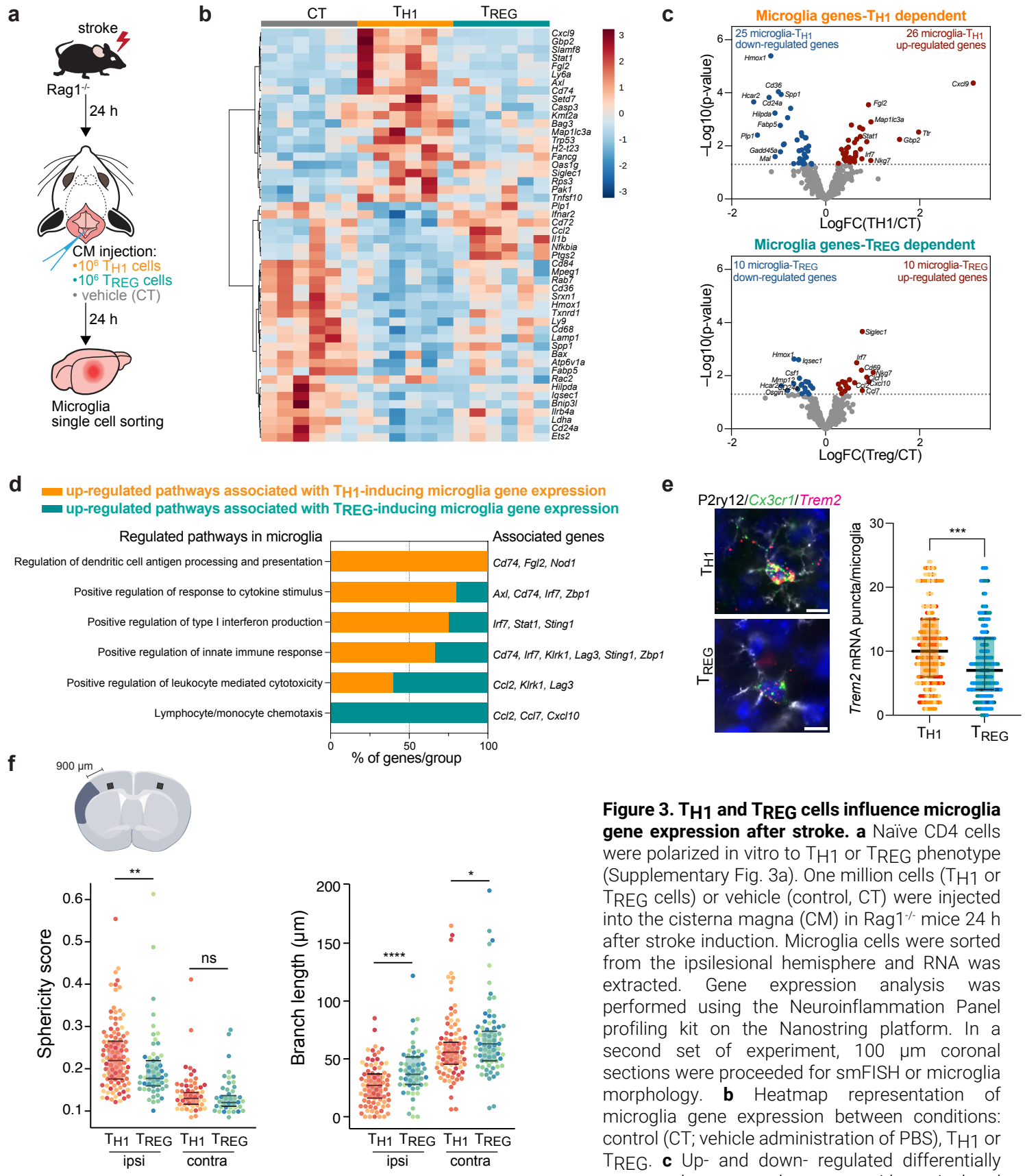


### Figure 2. Analysis of microglia isolated from WT and *Rag1*<sup>-/-</sup> in naïve and stroke conditions using the Smart-Seq2 platform.

**a** Correlation between the 291 pools of microglia. Hierarchical clustering identified 7 clusters, named from S1 to S7. The amount of samples is in between parentheses. The 1000 most variable genes were considered. The color represents the Pearson correlation coefficient between the samples. **b-d** UMAP plots showing the samples colored by clusters (b), genotype (c) and condition (d) and their associated cell distribution of genotypes and conditions among the sample clusters. **e** Average expression of gene clusters (defined in panel g) within each sample cluster. Scale is the average of the log normalized expression. **f** Box plots of the gene clusters in each conditions and genotypes. Grey boxes highlight significant difference between WT and *Rag1*<sup>-/-</sup> in stroke condition. \*, P < 0.05; \*\*, P < 0.01; \*\*\*, P < 0.001. Nonparametric Kruskal Wallis test followed by multiple non-parametric Wilcoxon t-tests and Bonferroni post-hoc correction for multiple testing. **g** Gene clusters and associated pathway enrichment analysis. Hierarchical clustering identified 7 gene clusters, named G1 to G7, only the significantly regulated gene clusters G1 and G3 between WT and *Rag1*<sup>-/-</sup> in stroke condition are shown. Each barplot shows the pathway enrichment analysis for the genes included in the gene clusters.

analysis. Hierarchical clustering identified 7 gene clusters, named G1 to G7, only the significantly regulated gene clusters G1 and G3 between WT and *Rag1*<sup>-/-</sup> in stroke condition are shown. Each barplot shows the pathway enrichment analysis for the genes included in the gene clusters.



microglia from TH1- (top) and TREG- (bottom) treated *Rag1<sup>-/-</sup>* mice relative to control condition (microglia isolated from *Rag1<sup>-/-</sup>* mice treated with vehicle, genes are color-coded accordingly to a p-value < 0.05 and |fold change| > 3). **d** Pathway analysis was performed for the up-regulated genes in each condition using the ClueGO package from Cytoscape. **e** Higher amount of *Trem2* mRNA puncta (red) per *Cx3cr1*-positive (green) in *P2ry12*-labelled microglia (white) in TH1-treated mice in comparison the TREG-treated mice. DAPI (blue) was used as nuclear dye. Scale bar = 10  $\mu$ m. **f** Morphological analysis of IBA1+ microglia in the ipsilateral (900  $\mu$ m distal to the infarct border, cortical layer 4) and contralateral hemisphere, as shown in the representative coronal section. Sphericity score and branch length ( $\mu$ m) of microglia treated with TH1 (orange) or TREG cells (green). Each individual mouse is represented in the plots by one color (3 mice/condition), each dot corresponds to one microglial cells; ns, non significant; \*, P < 0.05; \*\*, P < 0.01; \*\*\*\*, P < 0.0001. Wilcoxon rank sum test with continuity correction and Bonferroni post-hoc correction for multiple testing.

**Figure 3. TH1 and TREG cells influence microglia gene expression after stroke.** **a** Naïve CD4 cells were polarized in vitro to TH1 or TREG phenotype (Supplementary Fig. 3a). One million cells (TH1 or TREG cells) or vehicle (control, CT) were injected into the cisterna magna (CM) in *Rag1<sup>-/-</sup>* mice 24 h after stroke induction. Microglia cells were sorted from the ipsilesional hemisphere and RNA was extracted. Gene expression analysis was performed using the Neuroinflammation Panel profiling kit on the Nanostring platform. In a second set of experiment, 100  $\mu$ m coronal sections were proceeded for smFISH or microglia morphology. **b** Heatmap representation of microglia gene expression between conditions: control (CT; vehicle administration of PBS), TH1 or TREG. **c** Up- and down- regulated differentially expressed genes between either isolated

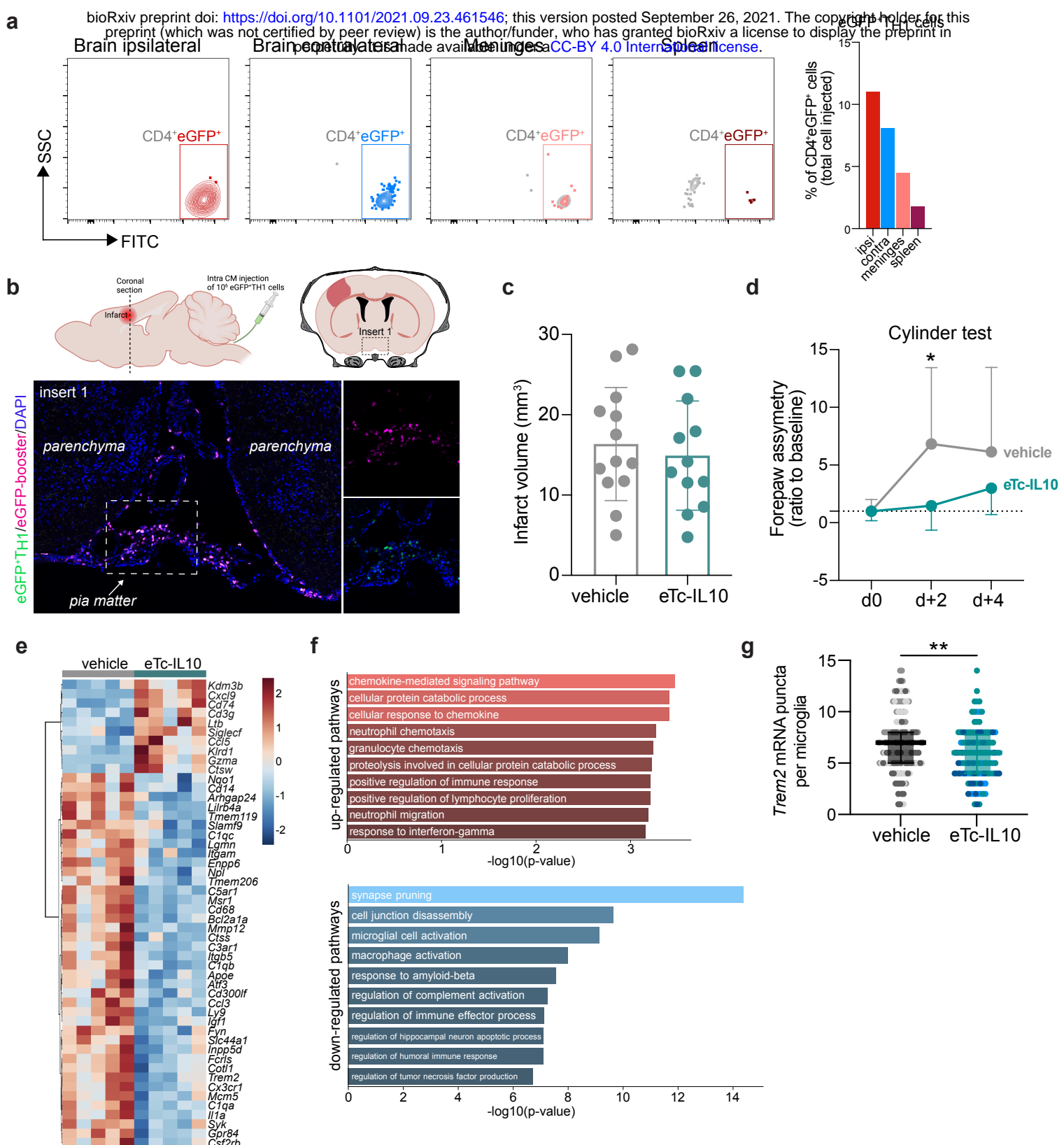


**Figure 4. Acute post-stroke treatment with engineered T cells overexpressing IL-10 modulates microglial activation and ameliorates functional deficit.** **a, b** Flow cytometry analysis and whole skull-brain coronal sections of  $10^6$  eGFP+TH1 cells injected into the cisterna magna (CM) of Rag1<sup>-/-</sup> mice 24 h after stroke. Samples were collected 4 h after CM injection for further analysis: **a** Flow cytometry plots showing CD4+eGFP+ cells isolated from the brain (ipsilateral and contralateral hemispheres), meninges and spleen (the detailed gating strategy is shown in Supplementary Fig. 3b). The graph represents the percentage of eGFP+TH1 cells relative to the total number of cells injected in the CM ( $10^6$  eGFP+TH1 cells). **b** Coronal section showing eGFP+TH1 cells in the meninges. Insert 1 indicates a representative photomicrograph of eGFP+TH1 cells counterstained with an eGFP-booster (magenta), cell nuclei are stained with DAPI (blue). The magnified images of white boxed area show eGFP+TH1 cells injected into the CM are located in the meninges. **c** Infarct volumes at 5 d after stroke in WT C57BL/6J mice treated by CM administration of either T cells secreting IL-10 (eTc-IL10,  $10^6$  naïve CD4+ cells transfected with a plasmid overexpressing IL-10, Supplementary Fig. 3c, d) or vehicle (aCSF) 4 h after stroke induction. **d** Percentage of assymetry in independent forepaw use ("0%" indicates symmetry) in mice treated with vehicle or eTc-IL10; \*, P < 0.05, ANOVA with Šídák's multiple comparisons test. **e** Heatmap representation of ipsilateral brain gene expression between vehicle and eTc-IL10 treated mice 5 d after stroke. **f** Selected gene ontology annotations for the 50 genes that were up-regulated (top) and down-regulated (bottom) in the whole ipsilateral brain tissue of eTc-IL10 treated mice in comparison to vehicle treated mice. **g** smFISH analysis of brains from eTc-IL10 treated mice showed a reduction of Trem2 mRNA puncta per Cx3cr1-positive microglia in the peri-infarct region in comparison to vehicle treated mice; \*\*, P < 0.01, Mann-Whitney U test.